

Jonathan Tschepe, Christian Navid Nayeri, Christian Oliver Paschereit

On the influence of Reynolds number and ground conditions on the scaling of the aerodynamic drag of trains

Open Access via institutional repository of Technische Universität Berlin

Document type

Journal article | Accepted version

(i. e. final author-created version that incorporates referee comments and is the version accepted for publication; also known as: Author's Accepted Manuscript (AAM), Final Draft, Postprint)

This version is available at

<https://doi.org/10.14279/depositonce-15351>

Citation details

Tschepe, J., Nayeri, C. N., & Paschereit, C. O. (2021). On the influence of Reynolds number and ground conditions on the scaling of the aerodynamic drag of trains. In *Journal of Wind Engineering and Industrial Aerodynamics* (Vol. 213, p. 104594). Elsevier BV. <https://doi.org/10.1016/j.jweia.2021.104594>.

Terms of use

This work is protected by copyright and/or related rights. You are free to use this work in any way permitted by the copyright and related rights legislation that applies to your usage. For other uses, you must obtain permission from the rights-holder(s).

Accepted Version

Corresponding author:

Jonathan Tschepe, Berliner Institut für Technologietransfer, Pascalstr. 10, 10578 Berlin, Germany, tschepe@bit-berlin.de

On the Influence of Reynolds Number and Ground Conditions on the Scaling of the Aerodynamic Drag of Trains

Jonathan Tschepe¹, Christian Navid Nayeri² and Christian Oliver Paschereit²

¹Berliner Institut für Technologietransfer, Berlin, Germany

²Chair of Fluid Dynamics, Hermann-Föttinger-Institut, Technische Universität Berlin, Germany

Abstract The present study examines the possibilities of transferring drag measurement results on reduced-scale train models to the respective full-scale vehicle. A comprehensive experimental and numerical study of the boundary layer and skin friction along trains is performed, focusing on REYNOLDS number effects. The data are supplemented by an extensive literature study and compared with different approaches from flat plate theory. Good agreement can be found when using the appropriate empiric coefficients and boundary conditions. Simultaneously, the difficulties in determining the skin friction drag of trains due to three-dimensional effects and surface roughness become apparent. The ground simulation analysis, including the effects of ground roughness due to ballast and sleepers, reveals a significant effect of the ground conditions on the vehicle's aerodynamic drag. Additionally, the effects of elements mounted on the train roof are investigated for different upstream flow conditions. Finally, a scaling method is proposed to transfer drag results from model-scale to full-scale trains based on the findings.

Keywords: Drag, friction, boundary layer, Reynolds number, trains, aerodynamics

1 Introduction

Aiming to become a sustainable and economical transport mode, the energy consumption of rail vehicles has become increasingly important in recent years (Garcia, 2010) (Meyer, et al., 2008) (Yamamoto, 2015), which is also reflected in the increased consideration of life cycle costs (LCC) in tenders and bids (Möbius, et al., 2017) (Steuger, 2009). Depending on the shape and velocity of trains, their aerodynamic resistance contributes a significant part to their energy consumption (Nolte & Würtenberger, 2003) (Lukaszewicz, 2009) (Lukaszewicz, 2007) (Orellano & Kirchhof, 2011) (Lai & Barkan, 2005) (Orellano & Sperling, 2009). Therefore, a precise prediction/determination of the aerodynamic drag of rail vehicles is necessary for both LCC analysis and energy saving. Different methods to determine the aerodynamic drag are described, for example, by Baker (2014) and Tschepe et al. (2019a). These methods can be divided into full-scale experiments, model-scale experiments, and numerical simulations. While full-scale experiments have their shortcomings in adaption in early project phases, numerical simulations, as well as scaled experiments,

can only reproduce the complex physics of the flow around trains to a certain extent (Baker, 2010). To predict the aerodynamic characteristics of trains using simulations or scaled experiments, the impact of the various boundary conditions needs to be analysed, and test setups need to be adapted accordingly. Even though studies regarding train aerodynamic drag have been performed for about a hundred years now (Davis, 1926) (Peters, 2008), the uncertainties from numerical simulations and reduced-scale experiments appear to be not sufficient to replace full-scale testing in case of drag verification (CEN, 2003). The present study compares the results of different model-scale experiments to full-scale results given by the literature, aiming at an improved understanding of the relevant boundary conditions for an accurate drag prediction of rail vehicles at model-scale.

This paper is structured as follows. Firstly, the introduction provides a review of the literature. Subsequently, an overview of the studies referred intensively within this work is given. The different experimental and numerical methods, as well as the investigated train model are presented in the third section. Afterwards, the results are presented, structured in the four categories boundary layer effects, frictional drag, pressure drag, and roof element analysis, followed by a concluding discussion.

1.1 Reynolds number impact

In order to transfer results from model-scale to full-scale, similarity must be granted. This includes geometric similarity as well as kinematic and dynamic similarity (Zohuri, 2015). The first requires an accurate replica of the object at a respective scale, while the others require similarity of streamlines and constant ratios of forces. While the requirement of precise scaled geometric details appears to be a minor problem in times of computer-aided design, 3D printing, and computerised numerical control milling (CNC), some questions arise from the representation of the correct train length. Since most trains feature train lengths more than 180 m (usually much more in case of freight trains), even at small scales of about 1:25 this results in a model length of at least 7 m, challenging the dimensions and quality of the test facility. The fulfilment of kinematic and dynamic similarity (taken together as mechanical similarity) for train aerodynamics, when assuming incompressible flow (i.e. train speeds below 350 km/h driving in the open), can be expressed by the REYNOLDS number $Re (\equiv UL_{ref}/\nu)$, U being the free-stream or driving velocity, L_{ref} a reference length of 3 m at full-scale and ν the fluid viscosity). Mechanical similarity is given in case of $Re_{model} = Re_{full-scale}$. Since the velocity of trains usually is in the range of 100-380 km/h, the corresponding REYNOLDS number is in the range of $Re=5\cdot 10^6$. As discussed by Tschepe et al. (2019a), using model scales of or below 1:20, the maximum REYNOLDS number is about $Re_{model}=1\cdot 10^6$, one order of magnitude below $Re_{full-scale}$ (not considering approaches of changing the fluid viscosity by cooling or pressure variation, as can be performed in wind tunnels, because this appears rather tricky for the moving model applications recommended in the following). Therefore, a detailed analysis of the impact of varying REYNOLDS number on the drag coefficient C_D is required ($C_D \equiv F_D/qA_{ref}$, with F_D being the drag force normalised by the dynamic pressure $q (\equiv \rho/2 U^2)$, ρ being the fluid's density) and the reference area A_{ref} , with $A_{ref}=10 \text{ m}^2$ at full-scale). This drag coefficient can be split into a pressure drag part $C_{D,p}$ and a frictional drag part $C_{D,f}$. Depending on the type and length of the train, the frictional drag varies from about 20% (relatively short and/or aerodynamically unfavourable trains, i.e. regional or freight trains) to 60% (long and smooth trains, i.e. high-speed trains) of the total aerodynamic drag (Nolte & Würtenberger, 2003) (Orellano & Kirchhof, 2011) (Peters, 1983). Besides the pressure loss at nose and tail, the pressure drag reflects repeated flow separations along the train, induced by inter-car gaps, bogies, or roof equipment (Peters, 1983). While the pressure drag coefficient is supposed to remain approximately constant above a certain critical

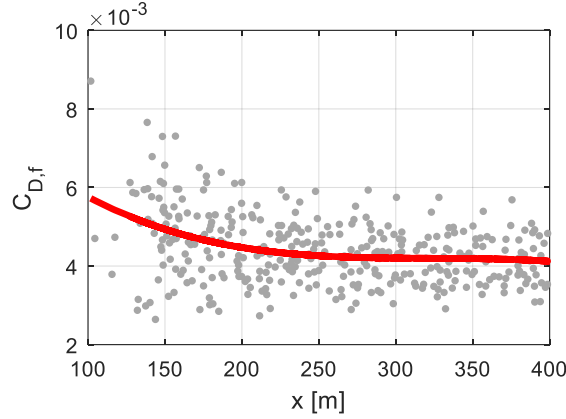


Figure 2: Skin friction drag coefficient $C_{D,f}$ ($\equiv F_f/(qA)$, with F_f being the frictional force and A the wetted surface)¹ measured for the Shinkansen Series0 (Maeda, et al., 1989) and resulting mean fit (red line)

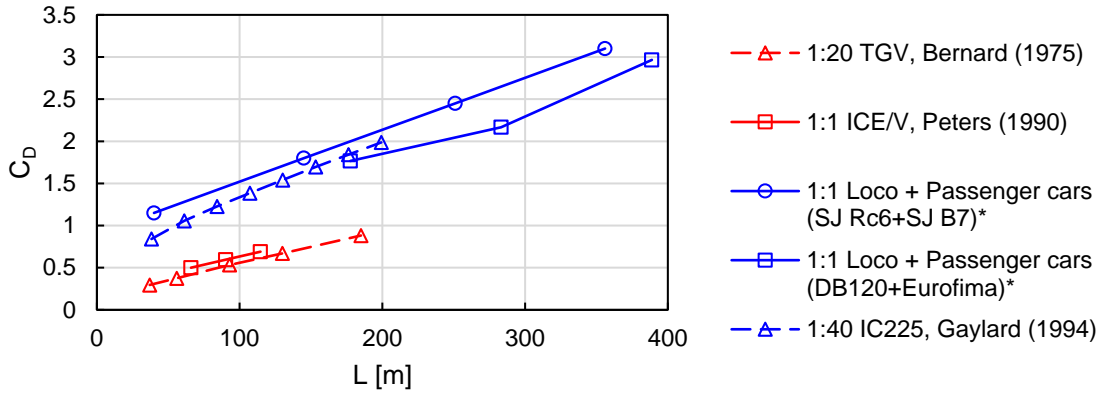


Figure 3: Drag coefficient plotted against train length according to Bernard (1995), Peters (1990), Gaylard et al. (1994), and *=Lukaszewicz (2009) based on $A_{ref}=10 \text{ m}^2$

Another observation, which sometimes is considered an indicator for a REYNOLDS number independent frictional drag (Hucho, 2012), is the linear correlation of the drag coefficient with the train length (Figure 3). However, when looking for drag coefficients of trains measured at more than two different length scales with realistic boundary conditions, i.e. full-scale test model-scale tests using a moving ground, the database becomes relatively small. Taking environmental effects (such as cross-wind in case of full-scale measurements) and measurement uncertainties into account, these observations do not appear to be a suitable reference for the evaluation of REYNOLDS number effects over a wide range.

From the above summary, it becomes evident that the frictional drag of trains needs to be investigated in more detail to gain an improved understanding of scaling properties. Therefore, the skin friction drag will be analysed in the present study, and different methods to evaluate its impact will be discussed.

¹ In (Maeda, Kinoshita, Kajiyama, & Tanemoto, 1989), the hydraulic skin friction coefficient λ is considered, which corresponds to $C_{D,f} = \lambda/4$.

1.3 Ground simulation

In the case of vehicles running in the open with no cross-winds, the flow speed equals the relative velocity between ground and vehicle. For the flow underneath the vehicle, this results in a Couette like flow situation. Instead, in a wind tunnel or water tunnel with no ground motion relative to the investigated object, the flow condition underneath the vehicle resembles a duct flow. The resulting energy losses due to frictional and blockage effects lower the flow speed in this region (Zhang, et al., 2016). Additionally, the boundary layer forming on the wind tunnel floor might cover large parts of the train and lower the bodyside underbelly friction drag. Consequently, the train underbody drag is reduced. Conversely, the low-energy flow underneath the vehicle is not able to fill the base region behind the vehicle in the same way as in a moving ground case, resulting in a downstream shift of the rear stagnation point and a lowered tail drag (Zhang, et al., 2016) (Lajos & Preszler, 1986) (Xia, et al., 2017). Considering the large amount of underbody drag found for trains (Nolte & Würtenberger, 2003) (Orellano & Kirchhof, 2011), it is not surprising that the first effect described appears to be the most significant one and measurements using a fixed ground plane exhibit much lower drag coefficients than measured on a moving ground (Gaylard, et al., 1994) (Kwon, et al., 2001) (Zhang, et al., 2016) (Fago, et al., 1991). However, all of these studies used a flat and smooth moving ground, which does not represent the real ground situation found under a train, i.e. the trackbed. The effect of this simplification has been investigated by Paz et al. (2017). They obtained about 15% higher drag coefficient when including sleepers into their simulation of the trackbed. Baker et al. (2019) present a collation of friction coefficients, measured on various trackbeds, showing a strong dependence on the track roughness. The 15% change in the drag coefficient found by Paz et al. (2017) may well reflect this ground effect. Another indicator for the importance of the ground roughness are the results presented by Rochard and Schmid (2000), stating a 7% lower drag coefficient for a *Shinkansen* on a slab track than on a conventional trackbed.

The present work investigates the impact of ground effects and discusses possible approaches to transfer data measured on smooth grounds to rough grounds. In contrast to the moving ground, rotating wheels seem to have no significant impact on the flow around the train (Peters, 1983) (Zhang, et al., 2016) (Wang, et al., 2018) and will not be further considered in this study.









1.4 Roof equipment









When studying the flow around (high-speed) trains, the roof equipment is often neglected in model-scale experiments and simulations, due to the difficulties associated with REYNOLDS number effects regarding protruding elements, such as pantographs and insulators (CEN, 2010). However, the roof equipment, especially for short trains, can make a significant proportion (~8%) of the overall drag coefficient (Peters, 1983) (Orellano & Kirchhof, 2011) (Gawthorpe, 1982) (Tschepe, et al., 2019b). Therefore, the current study further investigates the effect of the roof equipment on the train aerodynamics.

2 Reference cases

For deeper analyses of the respective quantities and scaling effects, the data of several studies were used in addition to the current measurements. The respective work and the trains studied are briefly presented in Table 1. In the following, all drag coefficients are scaled to a reference area of $A_{ref} = 10 \text{ m}^2$.

Table 1: Reference cases

Train [Pic Ref]	Picture	Scale, method	Topic	Reference
APT-E [P1]		1:1	Boundary layer	(Richards & Cooper, 1977) (Gawthorpe, 1978)
BB9291+UIC cars [P2]		1:1, exp.	Boundary layer	(Bernard, 1971)
CRH380A [P3]		1:8, CFD	Boundary layer, skin friction drag, total drag	(Jia, et al., 2017)
DB103+IC cars [P4]		1:1, exp.	Boundary layer	(King & Pfitzenmaier, 1985)
Generic train model [P5]		1:25, exp.	Boundary layer	(Buhr & Ehrenfried, 2017)
IC125+Mark III coach [P6]		1:1, 1:40, 1:76, exp.	Boundary layer, skin friction drag, total drag	(Baker & Brockie, 1991) (Brockie & Baker, 1990)
ICE 2 [P7]		1:1, exp.	Boundary layer	(Baker, et al., 2019) (RAPIDE, 2001)
ICE/V [P8]		1:1, exp.	Drag	(Peters, 1990)

KISS [P9]		1:1, exp.	Skin friction	(Haff, et al., 2016)
Mark I (MkI) coach [P10]		1:1, exp.	Skin friction	(Gawthorpe, 1978)
Railjet [P11]		1:1, exp.	Boundary layer	(Kapfenberger, et al., 2015) (Behrends, et al., 2017)
Shinkansen A (Series 700) [P12]		1:1, exp.	Boundary layer	(Takaishi & Ikeda, 2012)
Shinkansen B	unknown Series	1:1, exp.	Boundary layer	(Takaishi & Ikeda, 2012)
Shinkansen C	unknown Series	1:1, exp.	Boundary layer	(Sakuma, et al., 2010)
Shinkansen D (Series 0) [P13]		1:1, exp.	Skin friction drag	(Hara, et al., 1968) (Maeda, et al., 1989)
Shonan E-Train [P14]		1:1, exp.	Boundary layer	(Miki, et al., 1959)
TGV-A [P15]		1:1, 1:15, exp.	Boundary layer, skin friction	(Paradot, 2001)
TGV 001 [P16]		1:1, 1:20, exp.	Drag	(Baker & Brockie, 1991)(Bernard, 1995)

3 Experimental and numerical Setup

Different experiments and numerical simulations on a scaled high-speed train model were performed within this study. This section describes the experimental facilities and measurements techniques, the numerical setup, and the investigated train model.

3.1 Investigated train model

The investigated train model represents the three-car version of the *ICE/V* high-speed train (Peters, 1990) at 1:22 scale, with a height of $H = 0.174$ m and a length of $L = 3$ m. Different variants were investigated: a simple variant with a smooth roof and simplified bogies, and a complex variant with detailed bogies and different types of roof elements (Figure 4). Further description of the model is given in (Tschepe, et al., 2019a) and (Tschepe, et al., 2019c). In order to study the influence of a fixed laminar-turbulent transition (cf. Figure 1 and (Erm, et al., 2012)), all measurements were performed with and without a tripping tape (0.4 mm thick zig-zag tape) added to the train's front, as shown in Figure 5f. The size and position of the tape were derived from the literature (Fey, et al., 2013) (Erm, et al., 2012) (Tyll, et al., 1996).

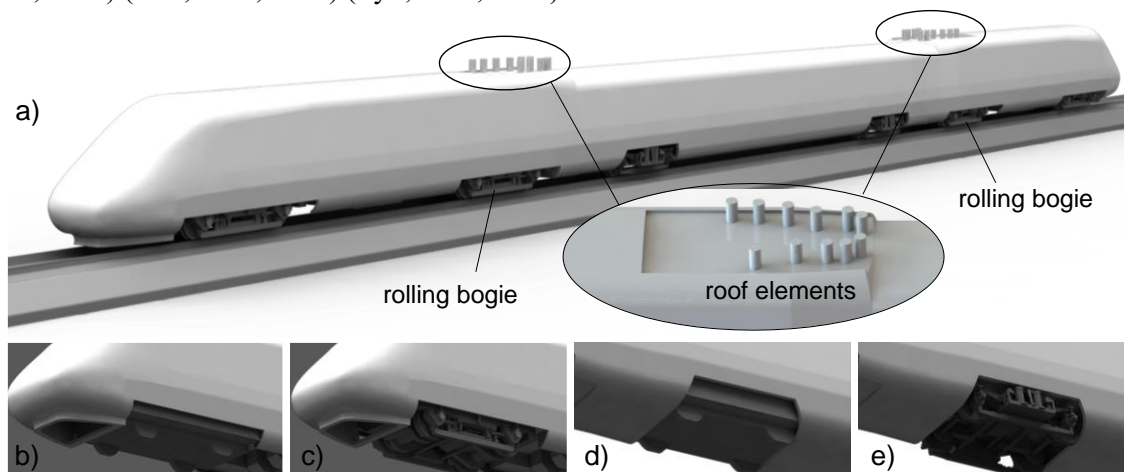


Figure 4: Investigated train model; **a)** complex variant with roof elements (for the simple variant, the roof elements were removed), **b)** simple endcar bogie, **c)** complex endcar bogie, **d)** simple midcar bogie, **e)** complex midcar bogie

3.2 Towing tank setup

Experiments on the effect of ground conditions were conducted in the shallow water towing tank of the *Technische Universität Berlin* (TUB), focusing on drag and skin friction measurements. A moving model rig was installed in the 120 m long, 8 m wide, and up to 1.1 m deep water tank, towing the train along the rail by using a thin rope inside the trackbed (Figure 5a, b). Two of the six bogies of the single-body train model were equipped with rolling wheels (Figure 4). All other wheels were cut 2 mm above the rail to avoid contact (Figure 5e). An internal force sensor of type

HBM S9M with ± 2 kN range and 0.01% resolution connected to the rope measured the running resistance. The aerodynamic drag was calculated by subtracting all forces beside fluid forces (i.e. rolling and wave resistance) from the measured towing force. In order to determine the running resistance and REYNOLDS number impact, the tests were performed at velocities ranging from $U = 0.15$ m/s to $U = 7$ m/s. However, due to the influence of surface waves (Tschepe, et al., 2019a), only velocities $U > 3$ m/s will be considered in the current study. A LabVIEW-based computer routine generated the required velocity profiles. A shaft encoder mounted to the winch and light barriers along the track detected the towing velocity. The wave resistance was calculated based on measurements of the water surface's elevation, as described in (Tschepe, et al., 2019a) and subtracted from the drag coefficient. Honeywell differential pressure sensors with a range of ± 7 kPa and ± 35 kPa and 0.5% resolution were used for surface pressure and PRESTON tube measurements. A further description of the setup, measurement techniques and drag determination methodology is given in (Tschepe, et al., 2019a).

The ballast and rails were designed based on (CEN, 2010), with deviations in the side slopes due to the use of standard elements, Figure 5b and 6b. In order to investigate the effect of ground roughness, the drag measurements were performed on a smooth ground (Figure 5b) and with additional roughness elements applied to the measurement section of the track, as shown in Figure 5c and d. Since the smooth ground setup corresponds to a slab track, the rail height was set to 220 mm at full-scale to represent the approximate ground clearance found for this track type (Kleeberg, 2009). The rough ground setup represented a track with ballast and sleepers. As the roughness elements had a height of 3 mm, the ground clearance, in this case, was about the same as given in (CEN, 2010), corresponding to a UIC60 rail. The characteristics of the boundary layer created by the elements were investigated in a small wind tunnel with a closed test section of 2 m length, a cross-section area of 0.55×0.55 m², and maximum wind speed of 25 m/s. A fishmouth probe (shown in Figure 16) was utilised to measure the boundary layer profiles 0.45 m downstream of the elements' position on a splitter-plate, assuring a fully developed boundary layer. The same tripping tape as applied on the train model (Figure 5f) was mounted at the tip of the splitter plate installed in the wind tunnel for fixed inflow conditions. According to full-scale investigations on the sand roughness k_s of trackbeds (Deeg, et al., 2008) (Soper, et al., 2017), $k_s = 0.1$ - 0.2 m can be assumed, which results in $k_s = 5$ - 10 mm at 1:22 scale. In order to create a respective roughness, different roughness elements were investigated, as will be discussed in section 4.2.2.

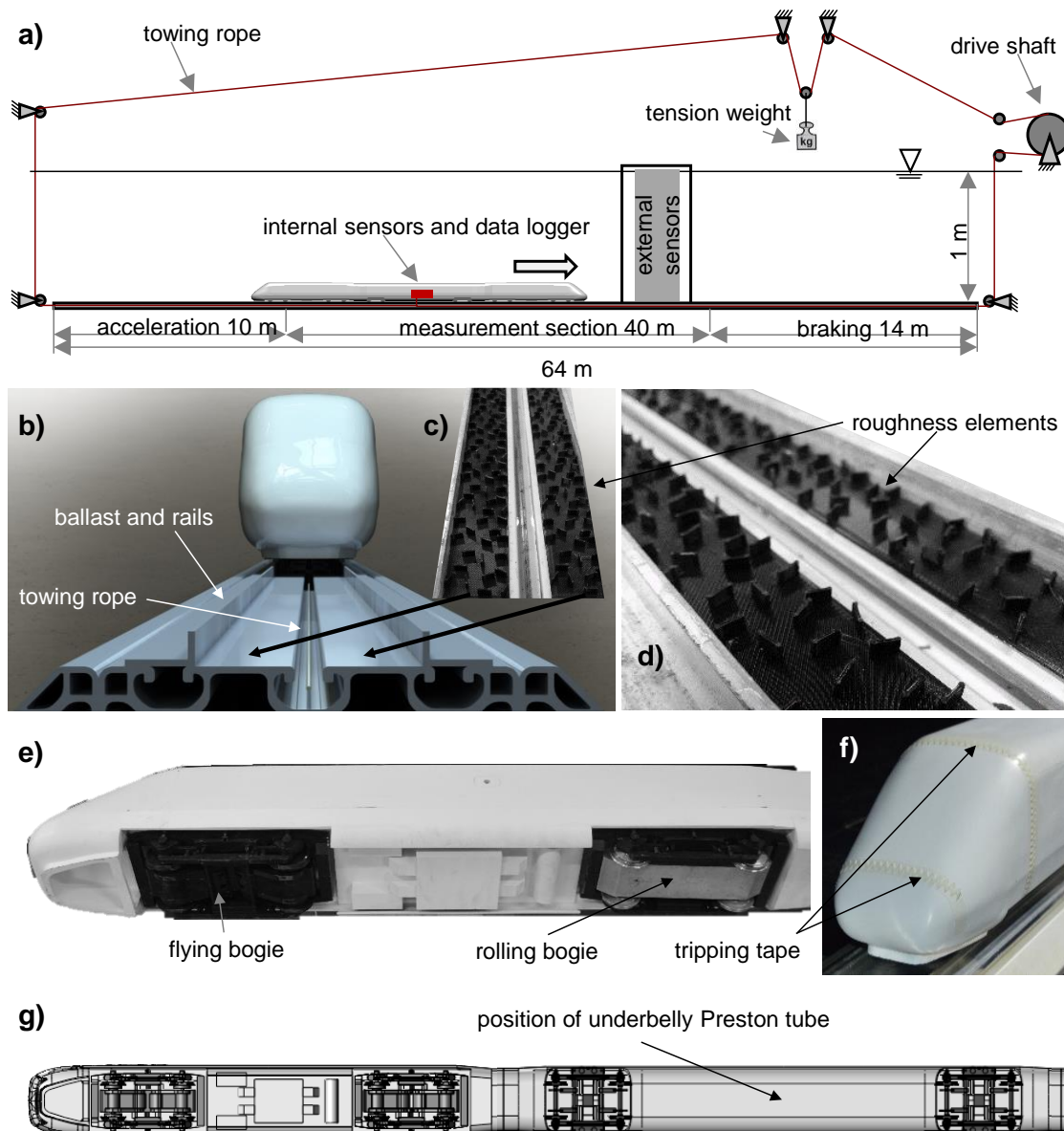


Figure 5: a) towing tank setup; b) towing rope inside the trackbed with smooth surface; c,d) roughness elements applied to the track; e) rolling bogie as implemented on the train's leading and tail car; f) tripping tape applied to the train's head; g) Preston tube position at the underbody of the train model

3.3 Wind tunnel setup

The wind tunnel measurements on the train model were performed in the large wind tunnel (GroWiKa) of the TUB. In addition to the drag and skin friction investigations, measurements regarding the train model's boundary layer profiles and wake flow were carried out. The GroWiKa is a closed-circuit wind tunnel, with a 5 m long test section, featuring a cross-sectional area of 1.4 m x 2 m (*height x width*). A splitter plate was used to generate a reproducible and small boundary layer (Figure 6a). An external six-component ballast was used for the measurement of aerodynamic forces and moments, with an accuracy of about 0.1 N and 0.15 Nm, respectively. All wheels

3.4 Numerical setup

Comparative CFD simulations for the same train geometries (simple and complex) were conducted using a Partially-Averaged-Navier-Stokes (PANS) approach for turbulence simulation implemented in *OpenFOAM* (Tschepe, et al., 2019c) (Fischer, et al., 2018a) (Fischer, et al., 2018b). The experimental setup was simulated including ballast, rails, moving ground, and the respective train models without further simplifications. A turbulence intensity of 1% was assumed at the inlet to match the experiments. The CFD domain and mesh is presented in Figure 7. For the simple and complex train variant, 13 Mio and 19 Mio cells were used, respectively. The near-wall flow was resolved by ten prism layers with a growth rate of 1.15, which allowed a wall-normal distance for the majority of cells of $y^+ = [25, 50]$. Hence, wall-functions based on the $k-\omega-SST$ wall-functions implemented in *OpenFOAM* were used to model the near-wall behaviour of turbulence. Simulations were conducted for $Re = 8.2 \cdot 10^5$, using the incompressible, transient solver *pimpleFoam*.

As described in (Tschepe, et al., 2019c), the CFD calculations using the PANS method represent a first attempt of this application to high-speed trains. The PANS results showed good agreement with the experimental data, thus justifying the comparison to data using the PANS approach. Since the numerical simulations are not the focus of this study but are merely used as an additional data source for comparison, and in order to save space, further details of the numerical approach (e.g., mesh sensitivity study) are not provided here. The obtained PANS results are very helpful to explain the relationships between boundary layer profiles and frictional drag.

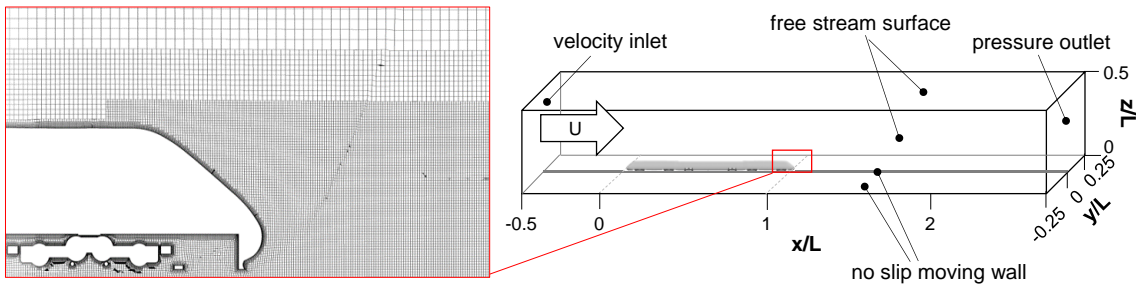


Figure 7: CFD domain and mesh around the trailing car

4 Results

This section provides the experimental and numerical results combined with supplementary data from the studies presented in Section 2. The results are structured into the topics of boundary layer investigations, an analysis of the frictional drag, including ground roughness effects, pressure drag investigations, and an evaluation of the impact of roof elements.

4.1 Boundary layer growth along flat plate and train

The frictional drag results from molecular and turbulent shear stress τ_w in the proximity of a body's surface and is closely connected to the flow profiles along the surface (Schlichting & Gersten, 2016). For a flat plate, the relevant turbulent boundary layer quantities, such as boundary layer profile and skin friction coefficients, can be calculated assuming a power-law function for the near-wall velocity profile with empirical quantities n and k (Schade, et al., 2013) (Prandtl, 2009).

From conservation laws, the boundary layer thickness δ_{99} (defined as the distance from the wall where $u(y = \delta_{99}) = 0.99 \cdot U$), as well as the local friction coefficient c_f , and the frictional drag coefficient $C_{D,f}$ for the smooth flat plate can be derived (see Appendix):

$$\frac{u(x, y)}{U} = \left(\frac{y}{\delta_{99}(x)} \right)^{\frac{1}{n}}, \quad (1)$$

$$\delta_{99}(x) = \left[C \left(\frac{1}{k} \right)^{\frac{2n}{n+1}} \right]^{\frac{n+1}{n+3}} x Re_x^{-\frac{2}{n+3}}, \quad (2)$$

with

$$C = \frac{(n+3)}{n \left(1 - \frac{n+1}{n+2} \right)}; \quad (3)$$

and

$$c_f = 2C^{-\frac{2}{n+3}} \left(\frac{1}{k} \right)^{\frac{2n}{n+3}} Re_x^{-\frac{2}{n+3}}, \quad (4)$$

$$C_{D,f}(L) = 2C^{-\frac{2}{n+3}} \left(\frac{1}{k} \right)^{\frac{2n}{n+3}} Re_L^{-\frac{2}{n+3}} \left(\frac{n+3}{n+1} \right), \quad (5)$$

where $Re_x \equiv Ux/\nu$ and $Re_L \equiv UL/\nu$. Here, x represents the streamwise location and L the length of the plate, i.e. $C_{D,f}$ represents the local friction coefficient c_f integrated over the length L .

For the flat plate, the above parameters often are calculated based on $n = 7$ (with $k = 8.74$ (Hucho, 2012) (Schade, et al., 2013)), which is therefore known as the *1/7 power law*. For large REYNOLDS numbers $Re_x \geq 3 \cdot 10^5$, however, it is expected that the flow profiles are more in line with a theoretical approach using higher values of n and k (Schlichting & Gersten, 2016) (Prandtl, 2009) (Schultz-Grunow, 1941), as shown in Table 2.

Table 2: Empirical coefficients n and k for theoretical boundary layer profiles at REYNOLDS numbers up to $Re = 2 \cdot 10^6$ according to (Schade, et al., 2013) and for higher Re_x as estimated by the author

Re_x	$4 \cdot 10^3$	$1.1 \cdot 10^5$	$3 \cdot 10^5$	$8.5 \cdot 10^5$	$2 \cdot 10^6$	$> 2 \cdot 10^6$	$\gg 2 \cdot 10^6$
n	6	7	8	9	10	11	12
k	7.75	8.74	9.71	10.6	11.5	12.4	13.3

The above power-law approach for a theoretical calculation of the boundary layer parameters has some shortcomings with regard to the fulfilment of physical boundary conditions at the wall (infinite slope) and the transition to the outer potential flow (not continuously differentiable), (Truckenbrodt, 2008). Therefore, another approach is the *law of the wake* approach, in which the boundary layer parameters are calculated based on empirical wake functions, as presented by Coles (1956) (Truckenbrodt, 2008) (White, 1991). The exponent of the REYNOLDS number term in these results indicates a similar dependence on the velocity as found for the *power-law* approach based on $n = 11$. When using the respective n and k (Table 2) to calculate the boundary layer quantities, it becomes apparent that, except the boundary layer thickness δ_{99} , all results agree quite well when comparing the *power-law* results with those from the *law of the wake* (Table 3). This accordance underlines the assumption that the power-law approach should consider values $n > 7$ in case of $Re_x \geq 3 \cdot 10^5$. Similar observations were made for the boundary layer on trains, where velocity profiles with $n = 8$ to $n = 12$ were found (Brockie & Baker, 1990) (Firchau, et al., 1980) (Neppert,

1984) (Bernard, 1971) (Miki, et al., 1959) (Sakuma, et al., 2010) (Crespi, et al., 1994) (Takaishi & Ikeda, 2012).

Table 3: Boundary layer quantities calculated using different semi-empiric approaches

Approach	δ_{99}	δ_1	δ_2	c_f	$C_{D,f}$
Law of the wake	$0.14 \cdot x \cdot Re_x^{-1/7}$	$0.0181 \cdot x \cdot Re_x^{-1/7}$	$0.0142 \cdot x \cdot Re_x^{-1/7}$	$0.0250 \cdot Re_x^{-1/7}$	$0.0303 \cdot Re_L^{-1/7}$
Power law ($n=11$)	$0.21 \cdot x \cdot Re_x^{-1/7}$	$0.0177 \cdot x \cdot Re_x^{-1/7}$	$0.0149 \cdot x \cdot Re_x^{-1/7}$	$0.0256 \cdot Re_x^{-1/7}$	$0.0299 \cdot Re_L^{-1/7}$
L/P	0.67	1.02	0.95	0.98	1.01

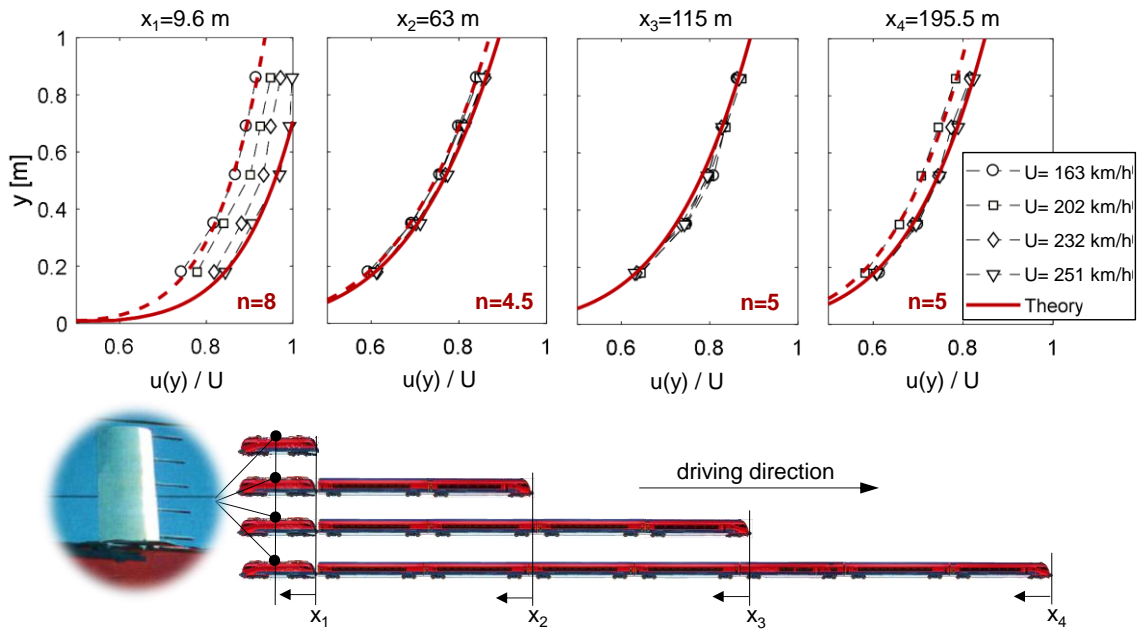


Figure 8: Boundary layer profiles measured on Railjet train in the open air using a pressure rake and theoretical approximation for highest (solid red line) and lowest (dashed red line) driving velocity

After the discussion on the generic flat plate boundary layer, the available database on full-scale train boundary layers is considered. Supplementary data from the studies by Kapfenberger et al. (2015) and Behrends et al. (2017) regarding the boundary layer in the open air are presented in Figure 8 for the Railjet train, by courtesy of HBI Haerter AG. The boundary layer was measured using a pressure rake installed on the loco, while the distance to the train's nose was varied by adding additional cars in front of the measurement position (Kapfenberger, et al., 2015). It can be observed that the boundary layer profile, when measured on the leading car, strongly depends on the driving velocity and thus the REYNOLDS number, similar as observed by King and Pfitzenmaier (1985). When adding cars upstream the measurement position, this dependency more or less disappears. However, in contrast to the findings presented above, n is found to be surprisingly low, with about $n = 5$. This discrepancy is probably due to the roof equipment, including the lowered pantograph, and the pronounced inter-car gap directly upstream the measurement position (cf. Figure 8 and (Kapfenberger, et al., 2015)), which reduces the flow momentum in the proximity of the wall. As can be inferred from Figure 9, a low near-wall momentum is better expressed by lower values of n .

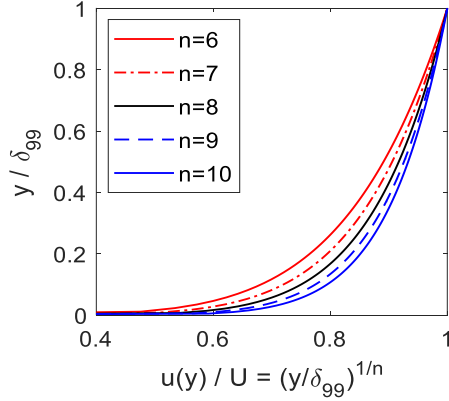


Figure 9: Theoretical boundary layer profiles for different values of n

The resulting theoretical boundary layer thickness δ_{99} along the *Railjet*, estimated by Eq. (1), as well as further data from other studies of train roof and side boundary layers, are presented in Figure 10. It can be seen that the boundary layer thickness in most cases indeed follows a progression of $n \geq 10$ for the power-law. This observation also applies to the *Railjet* and emphasises the differences between the flow development over the flat plate and a rugged surface such as a train

roof with roof equipment, since n for the boundary layer thickness (Figure 10a) does not correspond to n for the boundary layer shape (Figure 8). (Again, it must be noted that the profiles presented in Figure 8 were measured directly downstream the pantograph area and downstream the considerable inter-car gap between loco and coach, which will definitely have some impact on the boundary layer profiles.) Similar behaviour was observed for measurements downstream the pantograph on a *Shinkansen* by Takaishi (Takaishi & Ikeda, 2012) (*Shinkansen B* in Figure 10a). However, in case of no upstream roof equipment (*Shinkansen A*), the data agrees quite well with the theory for the respective n . Analogous behaviour can be observed for the boundary layer data measured on the train side in about 2 m height above the top of rail, Figure 10a.

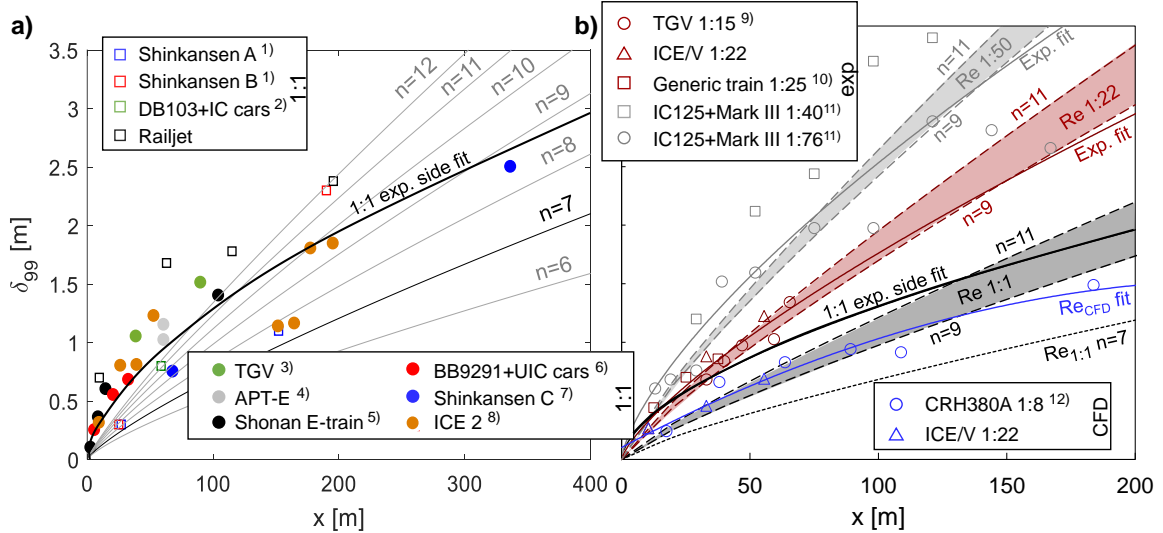


Figure 10: a) Boundary layer thickness from full-scale measurements on train roof (square marks) as given by ¹⁾(Takaishi & Ikeda, 2012) and ²⁾(King & Pfitzenmaier, 1985), as well as on the train side (round marks) as given by ³⁾(Paradot, 2001), ⁴⁾(Richards & Cooper, 1977) ⁵⁾(Miki, et al., 1959), ⁶⁾(Bernard, 1971), ⁷⁾(Sakuma, et al., 2010), and ⁸⁾(RAPIDE, 2001), and theoretical boundary layer thickness for different n (with k according to Table 2) for a velocity of $U= 250$ km/h; **b)** Boundary layer on train side (about 2 m above top of rail) from reduced-scale measurements at different REYNOLDS numbers and best fit compared to the theoretical boundary layer thickness using respective n and k for $Re_{1:1}=14 \cdot 10^6$ (according to **a**)), $Re_{1:22}=0.5 \cdot 10^6$ (representing red coloured model scale data), $Re_{1:50}=0.06 \cdot 10^6$ (representing grey coloured model scale data), and $Re_{CFD}=1 \cdot 10^6$ (representing blue coloured CFD data); experimental data as given by ⁹⁾(Paradot, et al., 2002), ¹⁰⁾(Buhr & Ehrenfried, 2017), ¹¹⁾(Brockie & Baker, 1990), and the current work, CFD results taken from ¹²⁾(Jia, et al., 2017)

Figure 10b shows experimental and numerical results for the boundary layer thickness at reduced scale. The best fit of the respective data is compared to the predicted theoretical boundary layer thickness with $n = 9-11$ for all REYNOLDS numbers, including the best fit resulting from the full-scale results presented in Figure 10a. It can be seen that the theory gives a reasonable estimate for all REYNOLDS numbers when using $n = 9-11$, while $n = 7$ results in an underestimated boundary layer thickness as exemplarily shown for the full-scale data. Figure 10b as well shows some boundary layer data from CFD investigations of high-speed trains, both using wall-functions (Tschepe, et al., 2019c) (Jia, et al., 2017). When comparing the CFD results to the experimental data, it can be seen that the simulation method of the near-wall flow chosen in these studies tends to underestimate the boundary layer thickness significantly. This effect will be discussed further in the following sections.

Baker (2010) points out that the boundary layer flow around a train is not two-dimensional and that self-similarity of the velocity profiles along a train is doubtful. While the latter is not even entirely the case on a flat plate, as can be concluded from the variation of n given in Table 2, the first point certainly causes some differences between the flow around a flat plate and a train. However, especially on smooth high-speed trains, the flow around the train should be dominated by the main flow direction at some distance to the ground. Therefore, as can be seen for the *Shinkansen C* data (Figure 10a), the agreement with flat plate theory is expected to increase for aerodynamically optimised trains, even though some differences will remain due the flow deflected to the train's roof (Baker, 2010). For less streamlined trains, Figure 10 shows that at the train's front, the boundary layer thickness increases much faster than on a flat plate, which is caused by flow separation at the head. The somewhat scattered data indicates the strong impact of the train's shape. It must be noted that all full-scale results contain some serious uncertainties since the measurement equipment, such as lasers or pressure-rakes, can only collect data in the near-wall region with a maximum wall distance of mostly below 0.5 m (Brockie & Baker, 1990) (Sakuma, et al., 2010) (Crespi, et al., 1994) (Takaishi & Ikeda, 2012). The smooth transition from the boundary layer velocity profile to the free stream or potential flow increases the uncertainties for defining δ_{99} , leading to an error band of about $\pm 40\%$ (Crespi, et al., 1994). Therefore, a more profound discussion probably would be possible using other boundary layer parameters, such as the displacement thickness δ_1 or the momentum thickness δ_2 (Baker, 2010). However, these quantities also are strongly affected by the small wall distance studied on full-scale trains and are often not presented by the authors.

Concluding, it can be said that the boundary layer along a train (at least at some distance to the ground) can be predicted to some degree by flat plate theory when using the correct empiric coefficients n and k for high REYNOLDS numbers. Furthermore, the REYNOLDS number seems to have a similar impact on the boundary layer thickness as known for the flat plate.

4.2 Frictional drag

4.2.1 Frictional drag at train side and roof

The frictional drag of the flat plate has been studied extensively (Hoerner, 1965) (Hucho, 2012) (Schlichting & Gersten, 2016) (Schultz-Grunow, 1941) (Truckenbrodt, 2008). Different formulae were derived from the above theories combined with empirical data to describe the frictional drag coefficient. Widely used are the formulae presented by Prandtl and Schlichting (2016), which take into account both the smooth and the rough flat plate:

$$c_{f,smooth} = (2 \cdot \log_{10} Re_x - 0.65)^{-2.3} \quad (6)$$

$$C_{D,f,smooth} = 0.455 \cdot (\log_{10} Re_L)^{-2.58} \quad (7)$$

$$c_{f,rough} = \left(2.87 + 1.58 \cdot \log_{10} \frac{x}{k_s} \right)^{-2.5} \quad (8)$$

$$C_{D,f,rough} = \left(1.89 + 1.62 \cdot \log_{10} \frac{L}{k_s} \right)^{-2.5} \quad (9)$$

with k_s representing the equivalent sand roughness of the surface (Schlichting & Gersten, 2016). As defined for Eq. (4) and (5), $C_{D,f}$ represents the local friction coefficient c_f integrated over the length L . Similar formulae were presented by Schultz-Grunow (1941) and Schoenherr (1932). The friction coefficient c_f based on these formulae is plotted against the REYNOLDS number in Figure 11. Since Eq. (8) and (9) do not depend on the REYNOLDS number, but only on the ratio x/k_s (or L/k_s , respectively), in case of $x/k_s = const.$, the skin friction coefficients are also constant. In this case, three different roughness regimes can be identified: One where the rough friction coefficient equals that of the smooth plate because the roughness is smaller than the viscous sublayer; One where the friction coefficient is constant (fully rough flow regime); and one in between. In the case of $U \cdot k_s = const.$, the roughness applies an offset to the smooth flat plate curve over the entire REYNOLDS number range. This correlation is particularly important when scaling the frictional drag of trains because it can be assumed that for model-scale and full-scale vehicle, the relation is more likely to be $U \cdot k_s = const.$ than $x/k_s = const.$ It implies that no such thing as a critical REYNOLDS number, above which the friction coefficient is constant, can be assumed for the skin friction drag.

Figure 11 further compares the friction coefficient for the smooth plate calculated according to Eq. (6) with the friction coefficients calculated based on the *power-law* (Eq. (4)) with different n and k . It can be seen that the Prandtl-Schlichting curve matches the different friction lines very well in the respective REYNOLDS number range given in Table 2, underlining the validity of the power-law approach when using correct empiric coefficients.

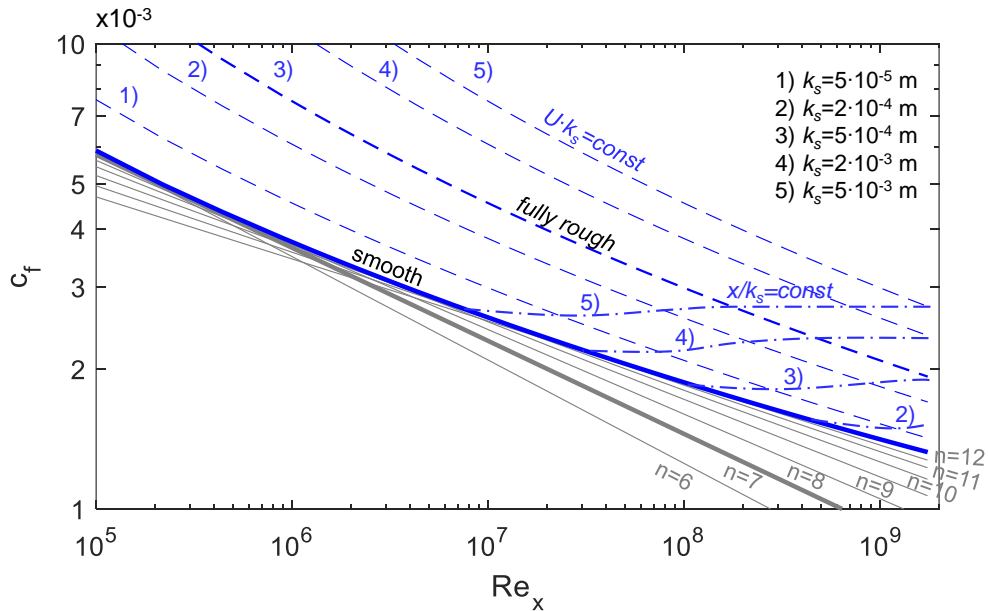


Figure 11: Friction lines for the smooth flat plate according to the power-law using different n (grey lines) and friction coefficient for the smooth and rough flat plate according to (Schlichting & Gersten, 2016); dashed lines indicate constant $U \cdot k_s$ (with $x=1-400$ m), dashed-dotted lines indicate constant x/k_s (with $U=1-70$ m/s); the fat blue line represents the Prandtl-Schlichting formula for the smooth flat plate

Friction coefficients measured on the train side are plotted in Figure 12a. A similar trend as for the flat plate can be observed. However, different than might be expected, some of the skin friction data measured on full-scale trains are below the one of the smooth flat plate. Baker (Brockie & Baker, 1990) (Baker, 2010) attributes this deviation to the three-dimensional flow effects around the vehicle. Besides, the difficulty of accurately determining the skin friction coefficient on non-smooth surfaces could also be an issue. The methods commonly used to determine skin friction, such as the PRESTON tube method or the CLAUSER diagram method (Tropea, et al., 2007), were developed or calibrated for smooth walls. Surface roughness poses a challenge since it generates an “error in the origin” of the mean profile, due to the well-known downward shift of the inner normalised flow profile (Schlichting & Gersten, 2016). An iterative attempt to consider this effect is shown in Figure 13: The measured data are first compared only with the slope of the friction lines given by the CLAUSER chart, and after identifying the best match, the roughness factor k_s is used to shift the data to the correct origin. That way, both skin friction coefficient and surface roughness can be determined to a certain degree of accuracy. With about $k_s = 0.2$ mm for the high-speed train and $k_s = 0.7$ mm for the regional train (Figure 13), the results agree well with the values given by Gawthorpe² (1978) and Molland et al.³ (2011). This method was used to calculate skin friction both from data given in the literature and the current experiments (Figure 12). For the full-scale train data, this leads to significant differences when comparing the results to a single point approach as the PRESTON tube method. In the latter case, the results would coincide with the values given for the IC125 and KISS (Figure 12a). Therefore, it is likely that the low values determined for these trains are biased in the same way, i.e. the roughness impact is neglected. If the IC125 and the KISS data are excluded, good agreement to the flat plate skin friction can be found. The model-scale train data compares well with the smooth flat plate data, while the full-scale results implicate some roughness. Considering that the model trains usually exhibit a very smooth surface and do not include details like rivets, window frames, or similar, which are featured by full-scale trains, this consistency appears to be reasonable. Peters (1983) stated similar, postulating that the friction increase caused by the increased roughness on full-scale trains might compensate for the decrease due to REYNOLDS number effects compared with model scale measurements. However, even if the two effects might cancel out each other to a certain extent, the full-scale coefficients still appear to be lower than those for the model train. Another interesting observation in Figure 12a is the low friction coefficient of the *ICE/V* calculated by the CFD. The discrepancy to the experimental data can be explained by an analysis of the boundary layer profiles. While for the experiments the boundary layer profiles on the train side follow a shape of about $n = 9$, the CFD calculates an $n = 6$ profile. The skin friction coefficient of the CFD also matches the $n = 6$ results for the flat plate theory, whereas the experimental results again match $n = 9$ (Figure 12a).

A good agreement of experimental train data and flat plate theory can be observed for smooth train roofs as well (*Shinkansen A*, Figure 12b). However, already small steps on the roof, as found on the *ICE/V* (Figure 14b), create some flow disturbances which result in a lowered measured skin friction coefficient, Figure 12b. If roof elements are added upstream of the measurement position, the velocity profile is dominated by wake flow structures (Figure 14 and Figure 15), making an interpretation regarding the skin friction coefficient with the above methods impossible. Therefore, Figure 12b only presents the data for the simple *ICE/V* configuration. Similar behaviour can be

² for the Mark I coach $k_s = 0.5-0.9$ mm, for the APT-E $k_s = 0.1$ mm

³ for smooth marine paint on ships $k_s = 0.05-0.1$ mm

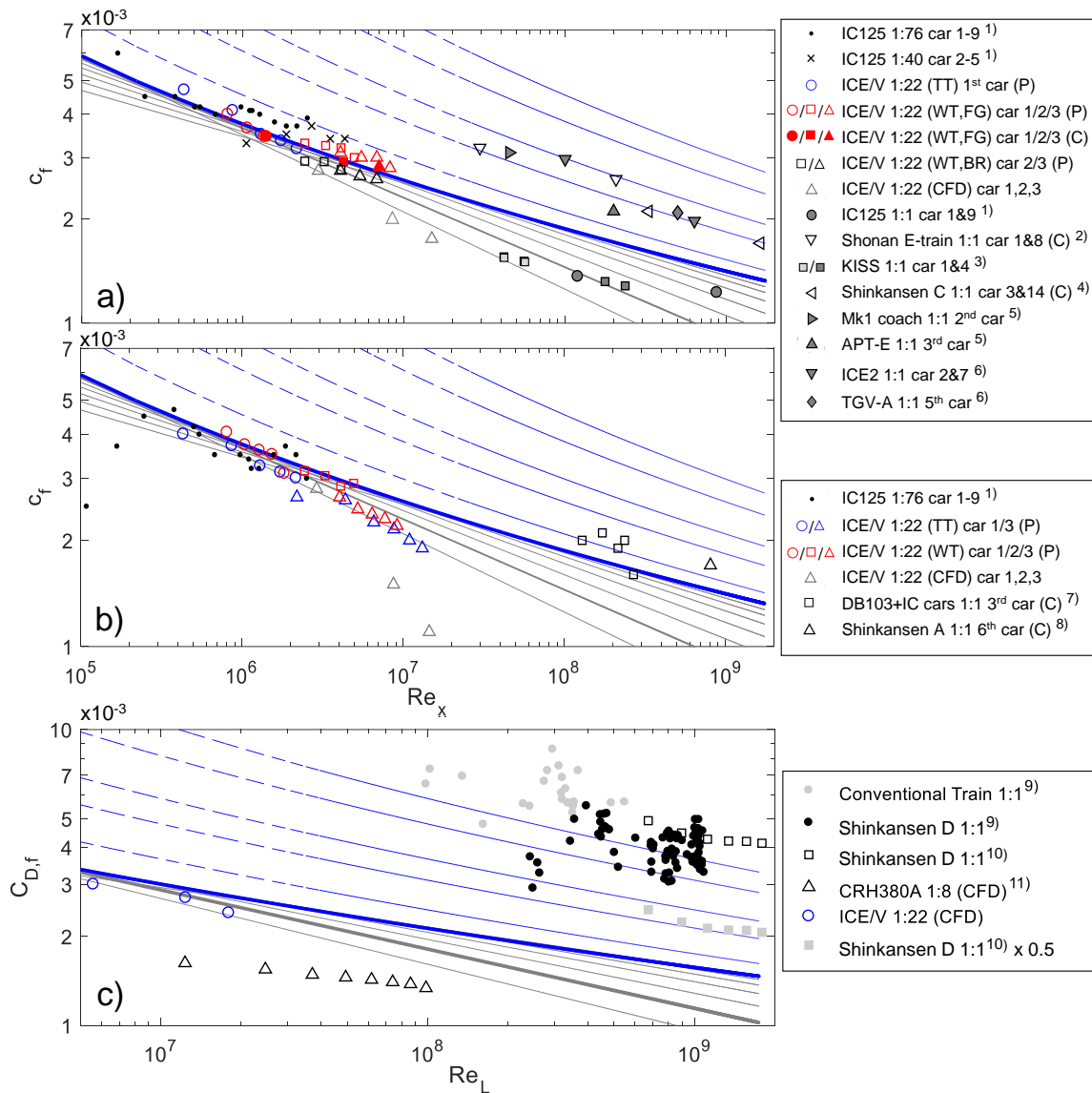


Figure 12: **a)** Skin friction coefficient measured on train side, according to ¹⁾(Brockie & Baker, 1990), ²⁾(Miki, et al., 1959), ³⁾(Haff, et al., 2016), ⁴⁾(Sakuma, et al., 2010), ⁵⁾(Gawthorpe, 1978), ⁶⁾(Baker, et al., 2019), and current measurements, evaluated using the PRESTON tube method (P) and CLAUSER chart method (C); **b)** skin friction coefficient measured on train roof according to ¹⁾ (Brockie & Baker, 1990) ⁷⁾(King & Pfitzenmaier, 1985), ⁸⁾(Takaishi & Ikeda, 2012), and current measurements; **c)** skin friction drag coefficient according to ⁹⁾ (Hara, et al., 1968), ¹⁰⁾ (Maeda, et al., 1989), and ¹¹⁾(Jia, et al., 2017)

observed for the data downstream the pantograph area of the *Railjet*, where the use of the CLAUSER chart method would lead to extremely high values of c_f and k_s , while the low near-wall momentum ($n = 5$, Figure 8) would result in a minimal skin friction coefficient. This discrepancy underlines the difficulties in determining a proper skin friction coefficient on complex bodies such as trains.

The model-scale roof data provided by Brockie and Baker (1990) shows another interesting flow feature: At the front end of the train, the drag coefficient drops significantly, indicating that the flow is not fully turbulent here. This observation agrees with the statement by Fey et al. (2013) that,

especially for aerodynamically optimised trains, some part of the first car is in a laminar flow condition (Figure 1). The current investigations were performed with and without tripping tape applied on the first car for a fixed laminar-turbulent transition. As can be seen in Figure 15a, the flow profile at the first measurement position is turbulent with and without tripping tape, and only some changes in the outer boundary layer region can be observed. Consequently, no differences in drag or skin friction coefficients were determined (less than 1% change) when adding the tripping tape. However, in the case of lower REYNOLDS numbers or better-streamlined heads, the flow around some part of the leading car can be laminar in model-scale testing (cf. Figure 1 and (Tyll, et al., 1996)), reducing its frictional drag in that region about 60-70%. Therefore, the use of a tripping tape is generally recommended. The laminar-turbulent transition further needs to be considered carefully when performing numerical simulations. When analysing the results presented in Figure 1, the position of the laminar-turbulent transition x appears to be in good agreement with flat plate theory $x_{plate} = 5 \cdot 10^5 \nu / U$ (Schlichting & Gersten, 2016) when adding a train-specific offset x_{nose} to account for pressure gradients at the train nose, leading to $x_{train} = x_{plate} + x_{nose}$.

Figure 12c shows a collation of the skin friction drag coefficient given for different trains. As mentioned before, the data provided by Hara (1965) are often used for justifying a REYNOLDS independent skin friction drag of trains. However, this interpretation shall be left to the reader. A clear trend showing REYNOLDS number dependency can be observed in the data given by Maeda et al. (1989) and Jia et al. (2017)⁴ and for the *ICE/V*. As observed when comparing the numerical and experimental data given in Figure 12a and b, the skin friction drag coefficients from the CFD in Figure 12c are below the ones for the flat plate. Again, this most likely results from the deviating boundary layer profiles compared to the experimental data (Figure 10) with smaller values of n in case of the CFD (the *ICE/V* coefficients again match with $n = 6$), probably due to the use of wall-functions at suboptimal boundary conditions. For the data given by Hara et al. (1968) and Maeda et al. (1989), it must be kept in mind, that this “frictional” drag as well contains some pressure drag components due to the applied methodology, i.e. all pressure drag except for head- and tail drag. Therefore, it is reasonable to assume that the train’s pure frictional drag will be about half of the frictional drag presented here, ending up in the flat plate range with $k_s \sim 0.2-0.5$ mm (Figure 12c). These results would be consistent with the observations from Figure 12a and b.

⁴ The data originally given by Jia et al. (2017) is referring to the cross-section area A . In order to normalize it with the wetted surface A_{wet} , the surface was estimated by $A_{wet} = \sqrt{A} \cdot L \cdot 4 \cdot 0.95$, as similarly proposed by Hucho (2012).

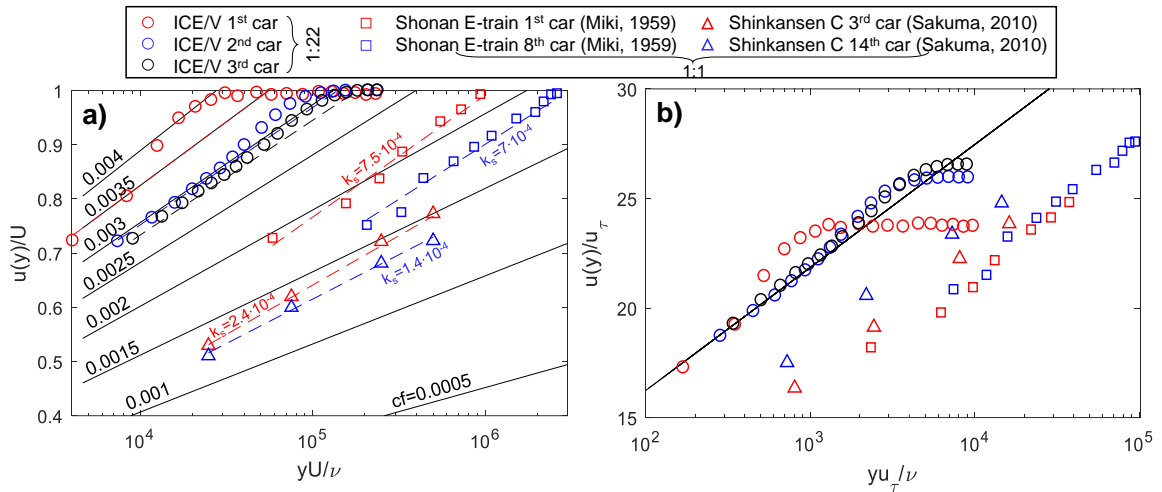


Figure 13: Boundary layer profiles measured on the train side a) displayed in the CLAUSER chart and b) compared to the smooth plate logarithmic law, calculated using $u(y)/u_\tau = \left(\frac{1}{\kappa} \log \left[\frac{yu_\tau}{\nu}\right] + 5\right)$ for the smooth plate and $u(y)/u_\tau = \left(\frac{1}{\kappa} \log \left[\frac{y}{k_s}\right] + 8\right)$ in case of roughness

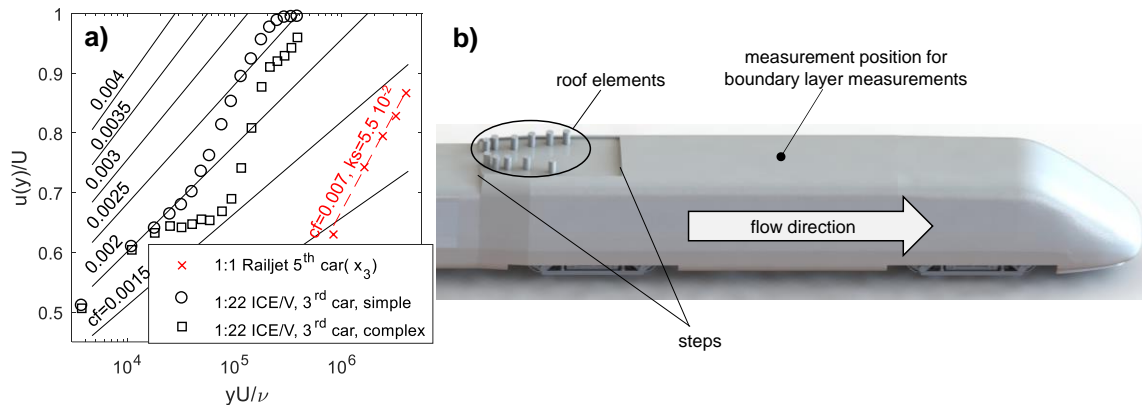


Figure 14: a) Boundary layer profiles measured on train roof displayed in the CLAUSER chart; b) ICE/V roof variant with roof elements (complex variant)

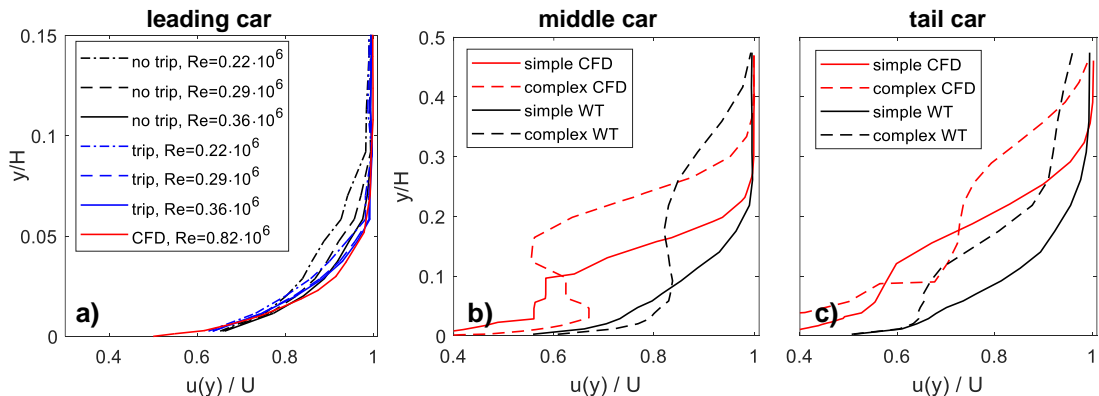


Figure 15: Boundary layer profiles on the 1:22 ICE/V roof on a) first car $x/L=0.16$ with and without tripping tape, b) middle car $x/L=0.5$, and c) last car $x/L=0.83$, measured in the wind tunnel (WT) and by CFD

4.2.2 Frictional drag at the train underbody

Concluding from Figure 12 it can be assumed, that, even though this is not covering the flow situation at all parts along the entire train correctly, the skin friction drag coefficient of trains behaves similar to the one of a flat plate. Therefore, model scale data should be scalable to full-scale REYNOLDS numbers when considering this aspect, as it is usually practised for ships and aeroplanes (Molland, et al., 2011) (Sforza, 2014). However, one region in the flow around trains needs a special consideration: the flow underneath the train. On the one hand, the boundary layer profiles in this region appear to be more or less constant (Deeg, et al., 2008) (Jönsson, et al., 2012b) (Soper, et al., 2018), indicating low REYNOLDS number effects. On the other hand, the trackbed is supposed to exhibit a high roughness and skin friction, at least in case of ballast and sleepers (Deeg, et al., 2008) (Soper, et al., 2017), which, due to equilibrium conditions, needs to be reflected in the skin friction of the train's underbody as well. In order to assess the underbody friction of a train accurately, the roughness of the trackbed must be taken into account. Most wind tunnel experiments, numerical simulations, and moving model tests use a smooth ground. On the one hand, because of the complexity of using a detailed trackbed with sleepers and ballast particles, on the other hand, because there is no standard for this detailed representation of the track. In the current experiments, the track roughness was not represented by an exact replication of sleepers and ballast particles at model scale but by using generic roughness elements as shown in Figure 16a-c, aiming at improved comparability with future measurements and numerical simulations. As described in section 3.2, a sand roughness of $ks = 5-10$ mm was aspired. Figure 16d shows the boundary layer profiles for the different roughness elements as obtained in the wind tunnel. The resulting coefficients of friction and sand roughness, identified as described in the previous section, are presented in Figure 16e and f.

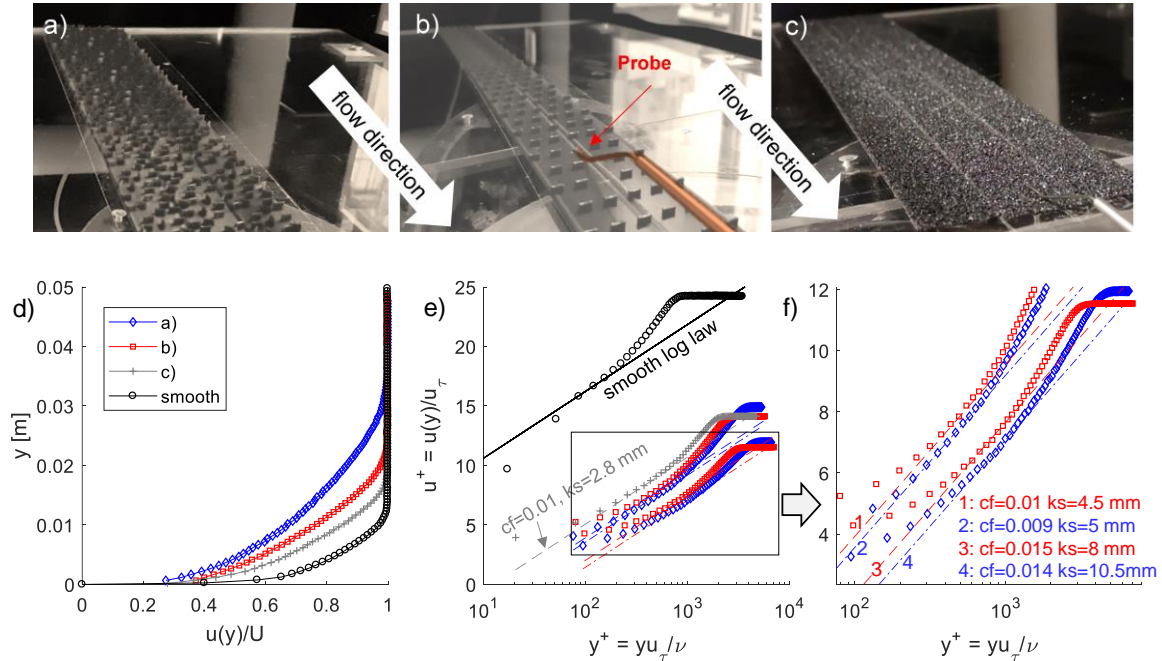


Figure 16: Roughness elements investigated in the wind tunnel: **a)** roughness elements arranged randomly, height 3 mm; **b)** roughness elements arranged according to (Schlichting & Gersten, 2016), Fig. 17.10, height 2 mm; **c)** sandpaper roughness grain size ~ 1 mm; **d)** resulting boundary layer profiles (with $y = 0$ set at the upper end of the investigated elements), and **e), f)** resulting friction coefficients and sand roughness

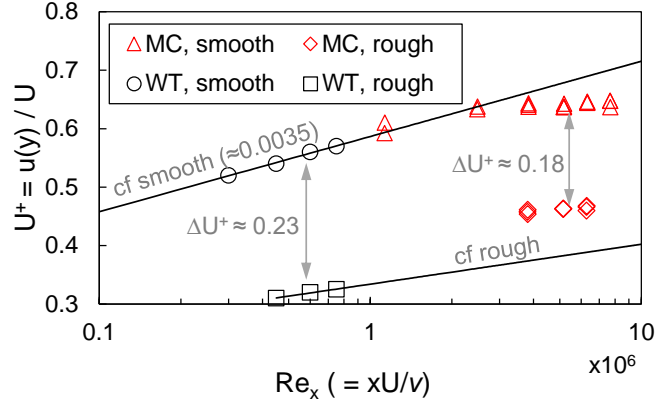


Figure 17: Normalised near-wall velocity measured for different REYNOLDS numbers and ground conditions above the ground in the wind tunnel (WT) and underneath the middle car (MC) of the 1:22 ICE/V in the towing tank

Since this method leaves a certain scope for interpretation, the solution for the roughness elements a) and b) is ambiguous, because two reasonable combinations of c_f and k_s match the experimental data in the logarithmic-law regime (Figure 16f). Eventually, the roughness elements presented in Figure 16a were used in the towing tank, assuming that their arrangement best represents the roughness produced by a real trackbed.

Figure 17 presents the normalised near-wall velocity measured in the towing tank by the PRESTON tube installed underneath the train's middle car, as shown in Figure 5g. Even though the data are not exactly matching the roughness lines identified by the wind tunnel measurements (note that the measurements may be influenced to some extent by the towing mechanism, as shown in Figure 5), the equilibrium effect can be well observed when comparing the downshift of the normalised velocity ΔU^+ in the presence of the roughness elements.

As discussed by Baker et al. (2019), the underbody roughness probably affects around 10-20% of the train's surface. A collation of different trains' drag coefficients obtained experimentally at model-scale and full-scale for the same train configuration, is shown in Figure 18a, combined with different attempts to scale the data. For the latter, the measured drag coefficient is split into a pressure part $C_{D,p}$ and a skin friction part $C_{D,f}$:

$$C_{D,measured} = C_{D,p} + C_{D,f} \cdot \frac{A_{wet}}{A_{ref}}. \quad (10)$$

For the calculation, the average of the measured drag coefficient and REYNOLDS number from the model scale experiments are used. Again, the wetted surface is estimated by $A_{wet} = \sqrt{A} \cdot L \cdot 4 \cdot 0.95$. The pressure and friction part now is calculated as follows:

1. the frictional drag is split into a smooth surface part $C_{D,f(smooth)}$ as expected for train sides and roof (Eq. (7)) and an underbody part with a constant⁵, i.e. REYNOLDS number independent, frictional drag $C_{D,f(underbody)}$:

$$C_{D,f(total)}(Re) = C_{D,f(smooth)}(Re) \cdot r + C_{D,f(underbody)} \cdot (1 - r), \quad (11)$$

with r being the ratio of side and roof surface to the total train surface. From Eq. (10), the pressure drag then becomes

$$C_{D,p} = C_{D,measured} - C_{D,f(total)}(Re_{model\ scale}) \cdot \frac{A_{wet}}{A_{ref}} \quad (12)$$

2. The respective drag coefficient for different REYNOLDS numbers now results from

⁵ note that in case of a constant friction coefficient $C_{D,f}=c_f$

$$C_D(Re) = C_{D,p} + C_{D,f(total)}(Re) \frac{A_{wet}}{A_{ref}} \quad (13)$$

In the following, different parameter settings will be considered and discussed. First, we consider the case of $r = 1$, where the flow at the train side/top and underneath the train is treated equally. As discussed above, this does not reflect well the flow conditions around the train, which is also indicated by the poor agreement of full-scale and up-scaled data shown in Figure 18 (red lines). A physically better approach is to assume a different friction coefficient in the underbody region, as expressed by Eq. (11). Since all measurements were performed using a smooth ground, $C_{D,f(underbody)} = 0.0035$ can be assumed, as observed for the smooth ground in Figure 17. Except for the IC125 (which may be due to measurement uncertainties), this gives a very good agreement of the experimental model-scale data and the theoretical approach over a wide range of REYNOLDS numbers. However, the full-scale results still are significantly underestimated. When considering the theoretical friction curves and the experimental model-scale data for increased underbody friction $C_{D,f(underbody)}$, it seems obvious that the discrepancies are due to the full-scale measurements been carried out on a rough trackbed instead of a smooth floor. The difference caused by the underbody skin friction drag for ballast and sleepers compared to the smooth ground seems to close the gap between full-scale and model-scale data and explains why scaling approaches omitting this effect often lead to an underestimation of up-scaled coefficients.

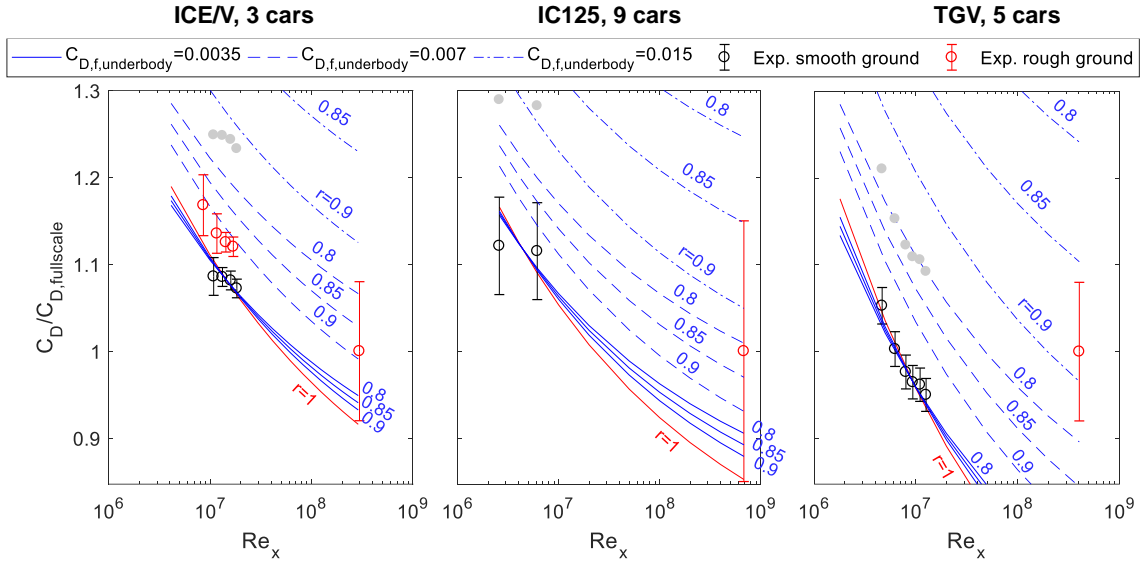


Figure 18: Measured drag coefficients and measurement uncertainties normalised by full-scale values - for the ICE/V according to the current results and full-scale results (Peters, 1990), for the IC125 according to (Brockie & Baker, 1990), and for the TGV according to (Baker & Brockie, 1991) and (Bernard, 1995). The blue lines represent the scaling approach according to Eq. (11)-(13) using different ratios r and different underbody friction coefficients $C_{D,f(underbody)}$, while the red lines represent the simple flat plate approach with $r = 1$. The grey dots represent the smooth ground experimental results increased by 15%, as found by (Paz, et al., 2017)

In the current experiments, the presence of the roughness elements increased the drag of the train model by about 4-5%. Investigations on the effect of sleepers on the drag of a three-car train performed by Paz et al. (2017) resulted in about 15% higher drag compared to the smooth BR ground setup. Besides the different types of ground roughness used, the lower drag increase observed in this study might as well be a result of the rugged underbody of the leading car and tail car (cf. Figure 5e and g). The smoother the train underbody, the stronger drag increase due to trackbed

roughness is to be expected. Hence, the drag increase depends on the percentage of underbody surface r , on the geometry/quality of the underbody (smooth or rugged surface), and on the roughness of the track $C_{D,f(track)}$. In the current experiments, the latter was found to be in the range of $C_{D,f(track)} = 0.009-0.014$ (Figure 16), so the maximum underbody friction in Figure 18 was set to $C_{D,f(underbody)} = 0.007-0.015$, assuming that $C_{D,f(underbody)} \sim C_{D,f(track)}$. It can be seen that higher underbody coefficients would result in an overestimated drag coefficient at full-scale (Figure 18). However, most track data presented by Baker et al. (2019) are in the range of $C_{D,f(track)} = 0.02-0.04$. Considering the implied skin friction drag of the train, it appears questionable that $C_{D,f(underbody)} = C_{D,f(track)}$. This discrepancy probably results from the fact that the effective friction on the train is the sum of actual friction and repeating pressure loss along the train (bogies, inter-car gaps, and elements mounted on the underbody), which must in some way be balanced by the track forces. Therefore, it can be assumed that the skin friction coefficient measured on the track is affected by the train underbody geometry in a similar way as the train underbody coefficient is affected by the ground roughness. Unfortunately, the ground roughness of the track under the influence of the train above was not measured in the current experiments. Hence, further investigations on the effect of ground roughness are required for a thorough understanding of the implications on the aerodynamic drag.

Figure 19 shows the percentage of the skin friction drag in the overall drag for the various parameter cases examined. According to the literature (Orellano & Kirchhof, 2011) (Nolte & Württenberger, 2003) (Peters, 1983) ratios of 30-50% are to be expected, which agrees well with the presented results. For the *TGV* the skin friction drag appears to be comparably high, with 60-75%. However, considering that the *TGV* in this configuration is 50% longer than the *ICE/V* but only has about 10% higher total drag, it is very likely that the *TGV* exhibits a very low pressure-drag⁶, increasing the proportion of frictional drag.

The analysis of the underbody friction leads to another interesting point. According to Figure 12, the skin friction drag coefficient on the train side and roof is about $C_{D,f} = 0.003$. The underbody friction coefficient presented in Figure 17 to Figure 19 is up to 5 times higher. Assuming that the underbody friction affects about 1/5 of the train's surface, the resulting drag is of similar magnitude to that created by the remaining surface. Therefore, for a high-speed train with about 50% of the total aerodynamic drag resulting from friction and half of this drag resulting from underbody friction, a reduction of the underbody friction by 50% would lower the overall aerodynamic drag by 12.5%. The dataset collected by Baker et al. (2019) and the results presented by Rochard and Schmid (2000) indicate that such reductions could result from the use of slab tracks instead of ballast and sleepers. These significant energy savings should be considered in future cost-benefit analysis for slab tracks from a systems perspective.

⁶ From the above made calculations, the pressure drag of the *TGV* is about $C_{D,p} = 0.16$, for the *ICE/V* $C_{D,p} = 0.30$, and for the *IC125* $C_{D,p} = 0.91$, only changing very little (<3%) with varying r .

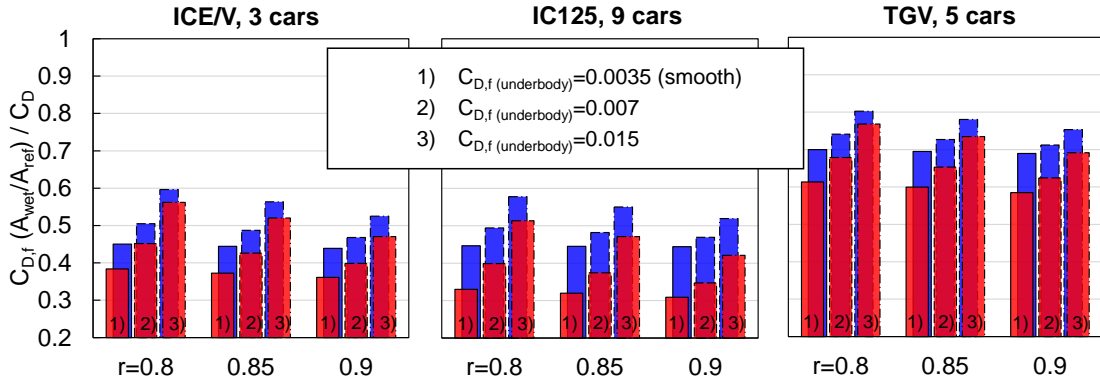


Figure 19: Percentage of total frictional drag in overall aerodynamic drag for various combinations of affected underbody surface r and underbody drag friction coefficient $C_{D,f, \text{underbody}}$ for model scale (blue) and full-scale (red), according to Eq. (11) and (13)

4.3 Pressure drag

4.3.1 Pressure gradients along the vehicle

The drag coefficient measured in a wind tunnel is generally affected by blockage effects (Willemsen, 1997) and a pressure gradient along the test section (Barlow, et al., 1999). While the former in case of small train models and angles of attack is rather low (for the current setup the blockage is $<2\%$) and can be easily corrected for by measuring the flow speed above the model (Figure 6a), the latter needs to be examined more closely. The static pressure in a closed wind tunnel (when no countermeasures are applied⁷) drops when moving in downstream direction along the test section due to the increased flow speed caused by the boundary layer growth along the wall. According to Barlow et al. (1999), for a closed square jet with width B the pressure loss can be estimated by

$$\Delta C_p(\Delta x) = -k \frac{\Delta x}{B}. \quad (14)$$

While Barlow et al. (1999) found k to be about $k = 0.016-0.04$, for the current setup k was identified to be $k = 0.054$ (with $B = \sqrt{A_{\text{test section}}}$). Similar to the correction method applied to the towing tank data to compensate for surface wave effects at lower velocities (for a detailed description see (Tschepe, et al., 2019a)), the drag coefficient can be corrected for the pressure change by

$$C_{D, \text{corr}} = C_{D, \text{meas}} + \Delta C_p(L). \quad (15)$$

For the three-car *ICE/V* train this gives $\Delta C_p \sim -0.1$, making more than 20% of the total drag coefficient (Figure 20). Even in a large wind tunnel with $B = 3$ m and small pressure loss, let's say $k = 0.02$, ΔC_p still would make 4-5% of the measured drag coefficient, increasing with increased train length. Thus, the pressure gradient in a wind tunnel appears extremely important to observe when performing drag measurements with long vehicles like trains. All wind tunnel data presented in the following were corrected in the described manner.

⁷ A common method to avoid pressure gradients is to alter the cross-sectional area along the test section, as performed for the measurements of the TGV presented in Figure 18.

4.3.2 Ground condition

Figure 20 shows the drag coefficient from the current study for the 1:22 *ICE/V* measured in the towing tank on the ballast and rail setup (with and without roughness elements) and in the wind tunnel on the ballast and rail and flat ground setup (Figure 5). It becomes apparent that the drag measured on the static ground in the wind tunnel is much lower (about 16% for the FG and 25% for the BR setup) than obtained with the moving model/ground in the towing tank and the CFD. The drag decrease when using a static ground setup agrees well with the observations by (Kwon, et al., 2001), (Gaylard, et al., 1994), and (Zhang, et al., 2016). Regarding the difference between static FG and BR setup, similar observations were made by (Schober, et al., 2010) and (Tomasini, et al., 2014). Comparing the towing tank results with the FG wind tunnel measurements, it can be seen that the absolute difference for the complex variant is higher than for the simple variant. This discrepancy is related to the reduced flow speed underneath the train in case of the static ground in the wind tunnel, which lowers the drag of the complex bogies and in general leads to a strongly distorted flow situation close to the ground (Zhang, et al., 2016).

Further changes related to the ground simulation occur in the train's boundary layer, Figure 21. While on the train roof, no alterations due to the ground simulation can be observed, significant changes occur on the train side, even though the measurement position is at about half the train's height, i.e. at some distance to the ground. The reduced flow speed underneath the train and at the lower train side also affects the tail car's pressure distribution, as shown in Figure 22. The static BR setup seems to have the strongest effect on the flow in ground proximity and creates significant differences in the pressure distribution compared to the moving model (Figure 22c). When increasing the ground clearance, the flow rate underneath the train and the according pressure distribution change (Figure 22a). This change also is reflected in the drag and lift coefficient, Figure 22d. Especially the lift coefficient shows a strong dependency on the ground clearance and for higher distances to the ground seems to approach the coefficients obtained by the CFD with a moving ground. Similar behaviour was observed by Fago et al. (1991) and Xia et al. (2017). The general discrepancy between FG and BR flow effects is supposed to result from a significantly increased boundary layer thickness on the BR setup ($\delta_{99} \approx 0.35H$ at $x/L=0.5$) compared to the FG setup ($\delta_{99} \approx 0.15H$ at $x/L=0.5$) due to flow separation at the upstream end of the ground setup. A similar effect on the tail car pressure can be assumed for varying roughness of the ground.

The above results show that both friction drag and pressure drag are affected by the ground simulation, i.e. the ground setup (FG or BR) and ground roughness. The impact of the ground clearance should as well be considered when analysing the effect of the investigated ground roughness as discussed above. In the current experiments, due to the height of the roughness elements, the ground clearance with applied roughness elements was slightly reduced, probably affecting the resulting drag coefficient.

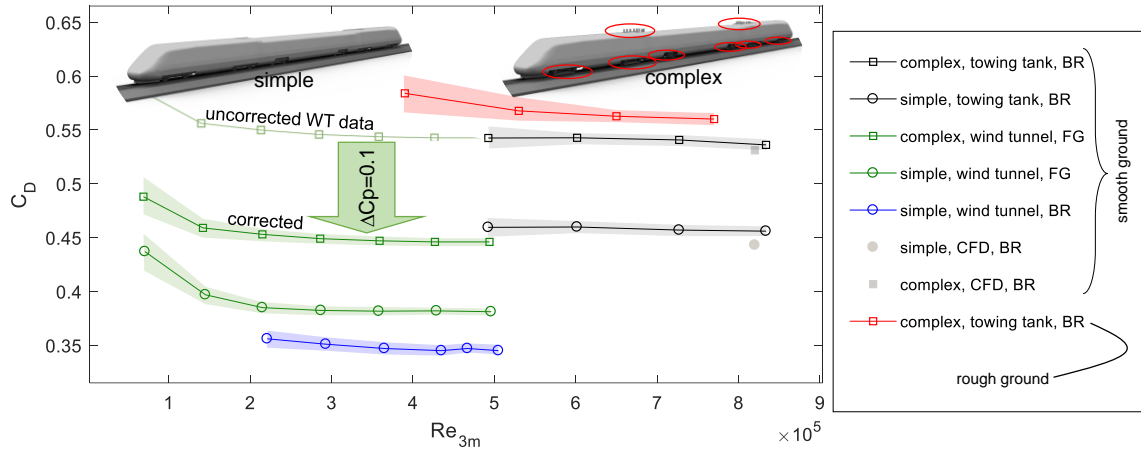


Figure 20: Drag coefficient and uncertainty range (transparent shading) for the 1:22 scale ICE/V plotted against the REYNOLDS number based on $L_{ref} = 3m$ at full-scale, measured on ballast and rail (BR) and flat ground (FG) setup

The wind tunnel results underline the sensitivity of the flow around a long vehicle in ground proximity towards ground boundary conditions. It can be clearly stated that drag investigations of trains on a static ground setup cannot in any way reproduce the flow physics around a moving train. Both static BR and FG setup do not appear to be useful for an overall drag prediction, with the BR setup being even worse, and should only be used to investigate flow effects on the roof. When using a moving ground setup, ballast (or at least an equivalent roughness simulation) and rails need to be modelled as well, as outlined in the previous section.

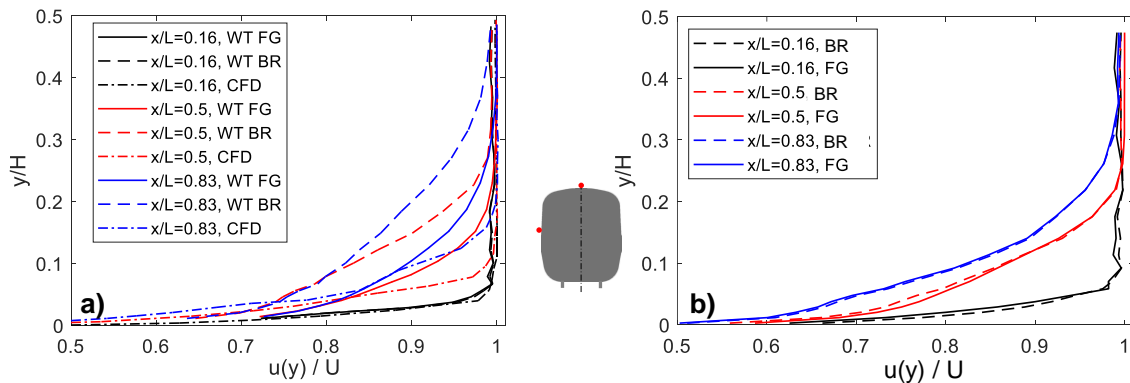


Figure 21: Boundary layer profiles of the 1:22 ICE/V at different positions along **a)** the train side and **b)** roof, as measured in the wind tunnel using a static flat ground (FG) and CFD using a moving ground with BR setup

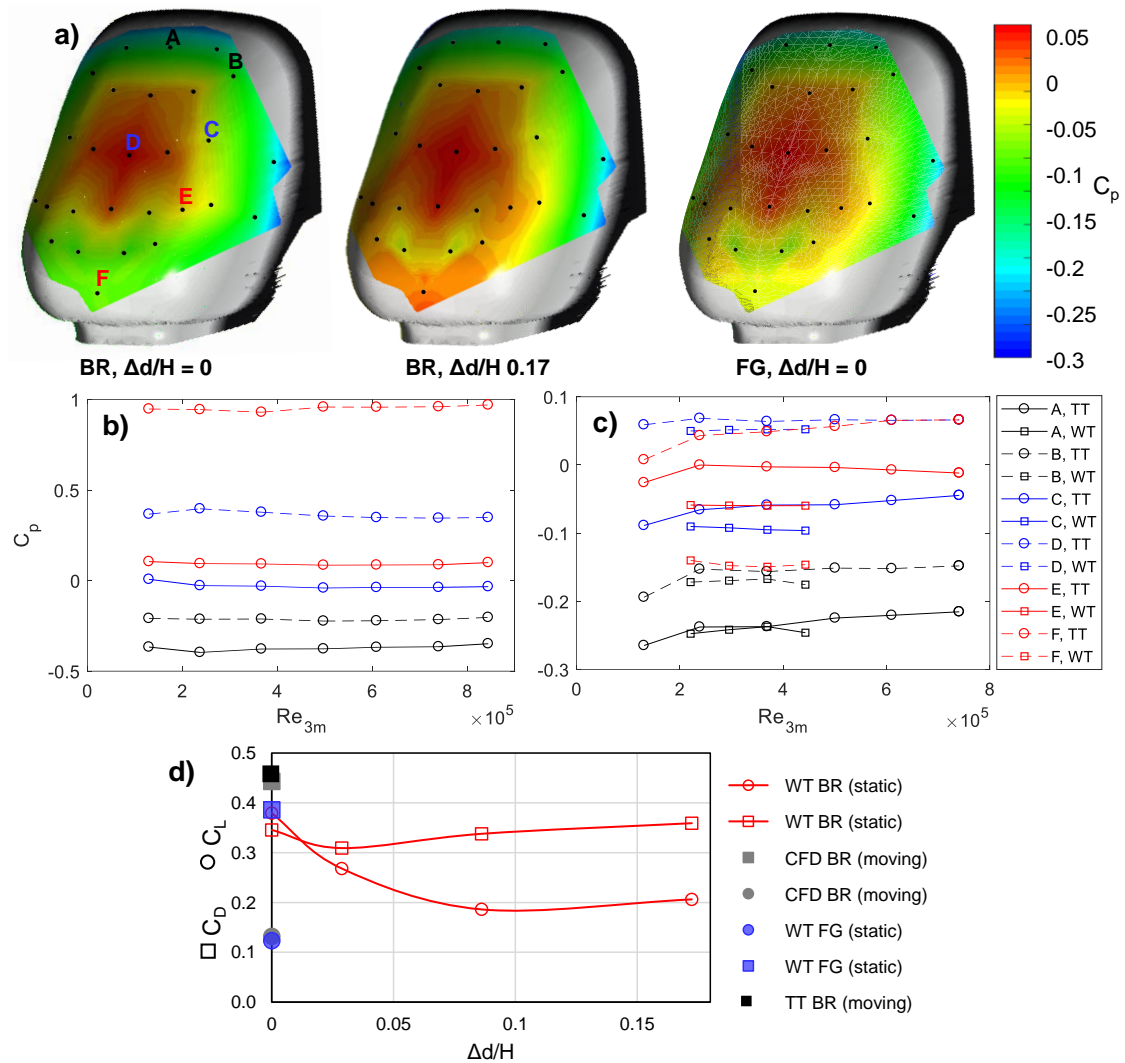


Figure 22: Pressure coefficient for the 1:22 ICE/V measured on **a)** the train's tail in the wind tunnel with different ground setups and ground clearances, **b)** the train's front in the towing tank, and **c)** the train's tail in the towing tank and wind tunnel on BR ground setup. **d):** Drag and lift coefficient obtained for the simple ICE/V model in the wind tunnel for different ground clearances

4.3.3 Reynolds number impact

Regarding the impact of the REYNOLDS number on the results, some further conclusions can be drawn from Figure 22b and c, where the pressure coefficient measured at the train's front and tail is plotted against the REYNOLDS number. While on the train's head the pressure distribution is not affected by the REYNOLDS number, some changes can be observed at the tail, indicating that constant pressure coefficients can only be expected for $Re > 0.4 \cdot 10^6$, which agrees with the observations made by (Niu, et al., 2016) and (Willemsen, 1997). Combined with the observations made for the drag coefficient in Figure 20, this leads to the conclusion that the pressure drag of streamlined trains can be considered as constant above REYNOLDS numbers of $Re = 0.4-0.5 \cdot 10^6$ and the drag coefficient then only is influenced by skin friction effects. However, for trains with more than three

or four cars, the boundary layer effects at reduced scale outlined in Section 4.1 and their influence on the tail pressure drag might shift this limit towards higher REYNOLDS numbers.

4.4 Roof elements

Figure 23 shows the drag increase due to elements added on the roof of the three-car *ICE/V* model. The additional drag caused by the elements strongly depends on their position on the train, i.e. the upstream boundary layer thickness. This effect is more pronounced for the cylinders (B1, B2) than for the pantograph (C1, C2) because the cylinders exhibit a lower height and are therefore more immersed into the boundary layer. As shown in Figure 10, the boundary layer thickness in scaled experiments exceeds the one found on full-scale trains due to REYNOLDS number effects. The velocity profiles expected on a full-scale and model-scale roof are shown in Figure 24. At both locations, the velocity integral up to the respective roof element's height is about 6% lower at model-scale, resulting in 12% lower drag forces.

In contrast to the aforementioned effect, it is well known from flow investigations of cylinders that the drag coefficient significantly reduces when exceeding a critical REYNOLDS number (Roshko, 1961). This also applies for inclined cylinders (Zurrel, 2004), which are more representative of a pantograph. A similar dependency of the drag coefficient on the REYNOLDS number was observed by Tschepe et al. (2019b) for insulators mounted on train roofs, reducing the drag coefficient in the (super-)critical REYNOLDS number range about 40% compared to the sub-critical one. In all cases, the critical REYNOLDS number, referring to the respective diameter, is $Re_D = 1\text{-}2 \cdot 10^5$. For a pantograph, where the largest parts, i.e. the upper and lower arm, exhibit a diameter of $D \approx 0.07$ m, the critical REYNOLDS number is attained at a driving speed of about $U = 160$ km/h. For insulators with diameters of $D = 0.1\text{-}0.2$ m, the critical REYNOLDS number is attained already at lower speeds. Thus, especially for high-speed trains, at full-scale, all elements on the roof can be expected to be in critical or super-critical flow condition, while at model-scale the flow condition will be sub-critical. Consequently, at model-scale, the coefficients will be overestimated compared to the full-scale. Although in some cases this effect might compensate the underestimation of the drag coefficient due to the upstream boundary layer thickness described above, such relation cannot be considered to be of general validity. When looking at the model-scale and full-scale pantograph drag from wind tunnel measurements presented in Figure 25, it appears that the REYNOLDS number effect only has minor effects on the pantograph drag, at least for the velocities plotted, i.e. below $U = 200$ km/h. A significantly higher influence results from the boundary layer thickness, as can be concluded from the investigations by Carnevale et al. (2016), which underlines the importance of an accurate boundary layer simulation when investigating elements on the train roof. For an accurate determination of the drag of roof elements, this might require a separate investigation with the boundary layer thickness adjusted accordingly, as performed by (Neppert, 1984), (Ido, 2015), or (Tschepe, et al., 2019b).

However, a separated investigation of train and roof elements has some shortcomings, because besides an impact on the drag coefficient, roof elements can completely alter the downstream flow field. When comparing the simple and complex roof configuration of the *ICE/V*, significant differences regarding the pressure distribution on the tail car were found (Tschepe, et al., 2019c). Similar deviations could also be observed in the wake of *ICE/V* in the wind tunnel, Figure 26. Here, due to the arrangement of the roof elements, the wake became less symmetric with the roof elements applied. When omitting elements on the roof, these downstream effects need to be kept in mind, for example, in the case of slipstream measurements.

The largest effect of insulators and pantographs can be expected on the otherwise smooth roofs of high-speed trains. Since there is a clear tendency on high-speed trains to cover everything except

the pantograph, soon the pantograph might be the only remaining component that requires special attention.

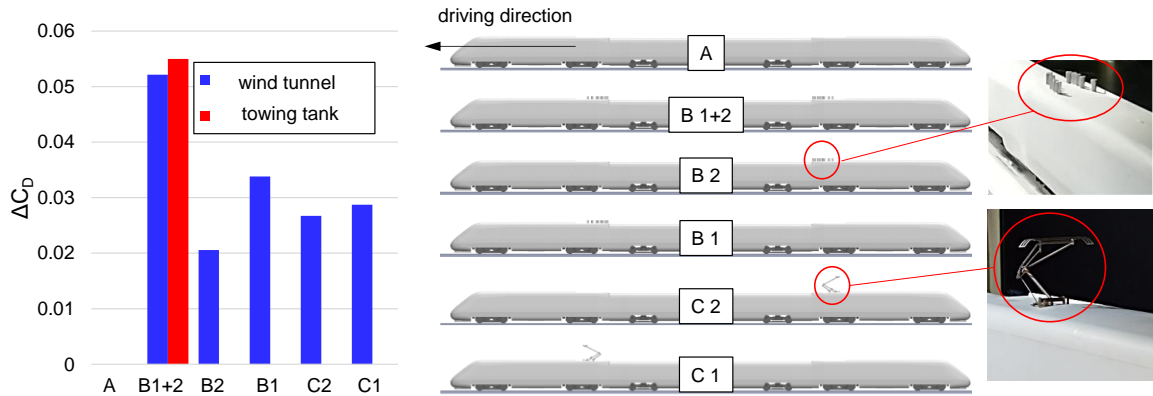


Figure 23: Drag increase due to elements mounted on the train roof of the 1:22 ICE/V

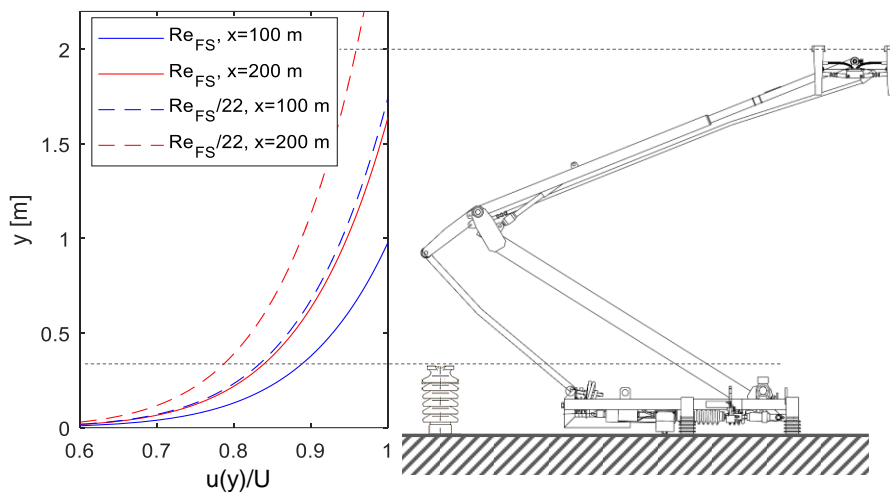


Figure 24: Boundary layer thickness and profiles according to the power-law using $n = 9$ at model-scale and full-scale REYNOLDS number

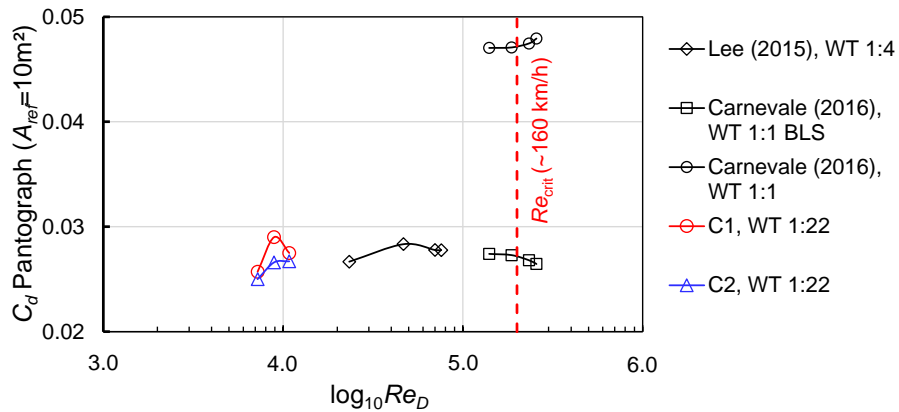


Figure 25: Drag coefficient of pantographs investigated in the wind tunnel and from (Lee, et al., 2015) and (Carnevale, et al., 2016) with and without upstream boundary layer simulation (BLS)

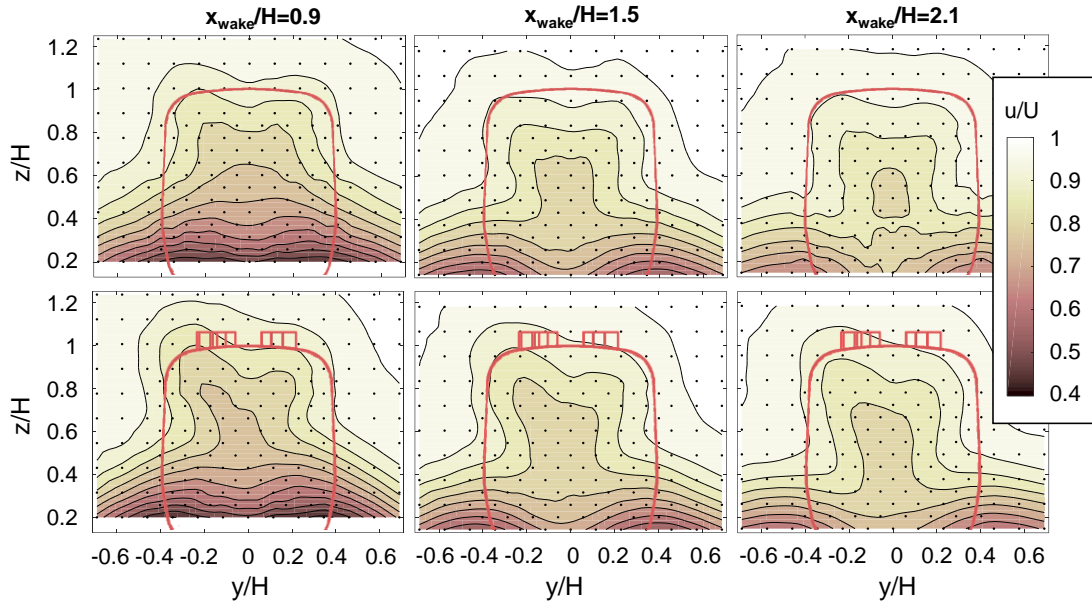


Figure 26: Streamwise velocity component u measured by the Omniprobe in the wake of the 1:22 ICE/V model in the wind tunnel on FG setup, with and without elements mounted on the roof

5 Conclusion

The present work examines various aspects of the scaling of drag coefficients measured on reduced scale train models. For this purpose, wind tunnel and towing tank experiments, as well as numerical simulations, were carried out. For appropriate comparability, all tests were performed at similar REYNOLDS numbers and setup specific influences such as surface waves (water channel) and blocking effects (wind tunnel) were subtracted. Nevertheless, some effects may be due to the peculiarities of the respective investigation method, which is why a large number of studies were consulted to compare and classify the values found.

The main challenges found are the REYNOLDS number and ground effects. The first one mainly affects the frictional drag. From the data presented, it can be concluded that the frictional drag of trains depends on the REYNOLDS number in a similar way as found for the flat plate. Due to the relatively small set of available full-scale measurement data, some uncertainties remain, especially since the skin friction determination on trains is anything but trivial. Based on a collation of different model-scale and full-scale measurements, it is shown that the classical *power-law* approach with $n = 7$ is not useful for the prediction of skin friction and boundary layer parameters along the train. However, a fairly good agreement is found for higher values of n , which also counts for the flat plate skin friction formulae given by PRANDTL. Therefore, a scaling approach based on these formulae is introduced and shows reasonable results. The simulation of the boundary layer and correct prediction of the skin friction drag also appear to be challenging for numerical simulations. For simulations without a fully resolved boundary layer, the skin friction drag is likely to be significantly underestimated.

The skin friction drag contribution is also part of the considerations regarding the correct modelling of the flow underneath the train. Experiments using a generic trackbed roughness revealed a high impact of the ground roughness on the train's underbody skin friction and drag coefficient.

Further experiments were conducted investigating the effect of static versus a moving ground. It is concluded that a realistic simulation of the flow underneath a train requires a moving ground in combination with an appropriate simulation of ballast and rails. The missing ground roughness in past studies and its effect on the flow under the train could be the reason for underestimated drag coefficients when scaling approaches based on friction effects were used. The current study presents an approach on how to transfer smooth ground drag coefficients to rough ground condition. However, further studies are required for validation. The most promising tool for such investigations appears to be the moving model facility, and further work to validate drag measurements using such facilities is highly encouraged. The interaction effects of train underbody and track conditions need a closer consideration in the future and might change the cost-benefit ratio of slab-tracks.

The pressure drag appears to be less sensitive towards the REYNOLDS number and for $Re \geq 4 \cdot 10^5$ probably can be considered constant for trainsets up to three or four cars. A more significant effect on the pressure distribution results from the ground setup (moving or static ground) and, in the case of wind tunnel measurements, pressure gradients along the test-section.

Finally, scaling issues resulting from the modelling of roof elements, such as pantographs and insulators, are investigated. It is shown that the REYNOLDS number has a doubled effect on the drag of these elements because it affects both the sub/super-critical flow condition and the upstream boundary layer thickness, and thus the flow momentum acting on the elements. The presence or absence of these elements is found to result in significant changes in the downstream flow pattern. Therefore, it seems questionable to simply omit such elements when studying train aerodynamics.

Concluding, for the scaling of drag measurements, the following aspects shall be highlighted:

- The tests need to be performed using a proper ground simulation, i.e. a moving ground or model with appropriate ground roughness.
- When using wind tunnels with closed test sections, the pressure gradient along the test section needs to be measured and the drag coefficient possibly needs to be corrected for the pressure gradient.
- A tripping tape at the train's head should be used for a fixed laminar-turbulent transition.
- The REYNOLDS number for reduced scale investigations (based on $L_{ref} = 3$ m at full-scale) should be $Re \geq 4 \cdot 10^5$ to achieve a constant pressure drag coefficient.
- The frictional drag at the train side and roof can be assumed to scale with the REYNOLDS number, similar as known for the flat plate. The underbody friction is more or less independent of the REYNOLDS number and strongly depends on the roughness of the trackbed.

Appendix

For a flat plate, the relevant turbulent boundary layer parameters can be calculated assuming a power law function for the near wall velocity profile:

$$\frac{U}{u_\tau(x)} = k \left(\frac{u_\tau(x) \delta(x)}{\nu} \right)^{\frac{1}{n}} \quad (\text{A1})$$

$$\frac{u(x, y)}{U} = \left(\frac{y}{\delta(x)} \right)^{\frac{1}{n}} \quad (\text{A2})$$

with empirical quantities k and n (Table 2), boundary layer thickness δ , and wall shear stress velocity u_τ ($\equiv \sqrt{\tau_W \rho}$). From conservation laws, the displacement thickness δ_1 and momentum thickness δ_2 can be derived:

$$\delta_1(x) = \int_0^\infty \left[1 - \frac{u(x, y)}{U} \right] dy \quad (\text{A3})$$

$$\delta_1(x) = \frac{\delta(x)}{n+1} \quad (\text{A4})$$

$$\delta_2(x) = \int_0^\infty \frac{u(x, y)}{U} \left[1 - \frac{u(x, y)}{U} \right] dy \quad (\text{A5})$$

$$\delta_2(x) = \frac{n \delta(x)}{(n+1)(n+2)} \quad (\text{A6})$$

From the definition of the wall shear stress velocity follows

$$\tau_W(x) = \rho u_\tau(x)^2 \quad (\text{A7})$$

and from momentum conservation

$$\tau_W(x) = \rho U^2 \frac{d\delta_2(x)}{dx}. \quad (\text{A8})$$

By equating these relationships, the boundary layer thickness δ can be calculated:

$$\delta(x) = \left[C \left(\frac{1}{k} \right)^{\frac{2n}{n+1}} \right]^{\frac{n+1}{n+3}} x Re_x^{-\frac{2}{n+3}} \quad (\text{A9})$$

with

$$C = \frac{(n+3)}{n \left(1 - \frac{n+1}{n+2} \right)}. \quad (\text{A10})$$

Using Eq. (A9), (A8), and (A6) this leads to

$$\tau_W(x) = \rho U^2 C^{-\frac{2}{n+3}} \left(\frac{1}{k} \right)^{\frac{2n}{n+3}} Re_x^{-\frac{2}{n+3}} \quad (\text{A11})$$

The local friction coefficient then is calculated by

$$c_f(x) = \frac{\tau_W}{\frac{\rho}{2} U^2}. \quad (\text{A12})$$

The frictional drag coefficient results from the frictional drag force, normalised by the dynamic pressure and the wetted surface (\equiv width b x Length L):

$$C_{D,f} = \frac{F_{D,f}}{\frac{\rho}{2} U^2 b L} \quad (\text{A13})$$

Using

$$F_{D,f} = b \int_0^L \tau_w(x) dx \quad (A14)$$

the frictional drag coefficient becomes

$$C_{D,f}(L) = 2 C^{-\frac{2}{n+3}} \left(\frac{1}{k}\right)^{\frac{2n}{n+3}} Re_L^{-\frac{2}{n+3}} \left(\frac{n+3}{n+1}\right). \quad (A15)$$

Acknowledgments:

The authors like to thank Prof. Chris Baker for the fruitful discussions and valuable input.

Conflict of interests: The authors declare that they have no conflict of interest.

Picture References

- [P1] https://en.wikipedia.org/wiki/British_Rail_APT-E#/media/File:ATP-E_IN_YARD.jpg
- [P2] <https://www.bahnbilder.de/bilder/die-bb-9291-sncf-gehorte-zu-889258.jpg>
- [P3] <https://www.hochgeschwindigkeitszuege.com/china/fotos-china/crh-380-a-expo-china-gr.jpg>
- [P4] <https://i.ytimg.com/vi/ue5qjWt0RtY/maxresdefault.jpg>
- [P5] (Buhr & Ehrenfried, 2017)
- [P6] https://upload.wikimedia.org/wikipedia/commons/thumb/d/dc/British_Rail_Class_43_at_Chesterfield.jpg/1200px-British_Rail_Class_43_at_Chesterfield.jpg
- [P7] https://upload.wikimedia.org/wikipedia/commons/3/34/ICE-2-Halbzug_Radbruch.jpg
- [P8] <https://img.webme.com/pic/e/eisenbahnen-db/ice0.jpg>
- [P9] https://www.deutschebahn.com/resource/image/4360352/stage-moderne-ikone/960/520/ebf24ace15a4c38e37cee96908dc6b98/vn/kiss_zug_1.jpg
- [P10] https://upload.wikimedia.org/wikipedia/commons/f/f5/British_Rail_Mk1_coach_number_99352.jpg
- [P11] https://upload.wikimedia.org/wikipedia/commons/2/2b/RJ_568.jpg
- [P12] <https://www.hochgeschwindigkeitszuege.com/japan/fotos-japan/jr-700-bild2-kl.jpg>
- [P13] <https://www.hochgeschwindigkeitszuege.com/japan/jr-baureihe-0.php?vor-gaengerdir=japan>
- [P14] https://en.wikipedia.org/wiki/115_series#/media/File:JR_East_115-1000_Ry%C5%8Dm%C5%8D-Line_6_cars.JPG
- [P15] https://fr.wikipe-dia.org/wiki/TGV_Atlantique#/media/Fichier:TGVA_n%C2%B0341_au_PN_401_bis_%C3%A0_La_Baule_par_Cramos.JPG
- [P16] <https://cdn.retours.eu/nl/36-tres-grande-vitesse-turbotrain-TGV/enlarge/TGV-001-Aquitaine-1973.jpg>

References

- Baker, C. (2010). The flow around high speed trains. *Journal of Wind Engineering and Industrial Aerodynamics*, 98, pp. 277-298, <http://dx.doi.org/10.1016/j.jweia.2009.11.002>.
- Baker, C. (2014). A review of train aerodynamics Part 2 - Applications. *The Aeronautical Journal*, 118(1202), pp. 345-382, <https://doi.org/10.1017%2Fs0001924000009179>.
- Baker, C., & Brockie, H. (1991). Wind tunnel tests to obtain train aerodynamic drag coefficients: Reynolds number and ground simulation effects. *Journal of Wind Engineering and Industrial Aerodynamics*, 38, pp. 23-28, [https://doi.org/10.1016/0167-6105\(91\)90024-Q](https://doi.org/10.1016/0167-6105(91)90024-Q).
- Baker, C., Johnson, T., Flynn, D., Hemida, H., Quinn, A., Soper, D., & Sterling, M. (2019). *Train Aerodynamics*. Oxford: Elsevier, <https://doi.org/10.1016/C2016-0-04444-3>.
- Barlow, J., Rae, W., & Pope, A. (1999). *Low-Speed Wind Tunnel Testing*. New York: JOHN WILEY & SONS, INC., ISBN 0-471-55774-9.
- Behrends, D., Dumitra, M., Flückiger, M., Heland, J., & Höregott, D. (2017). Stromabnahme unter dem Einfluss der Aerodynamik im Tunnel - Auswirkungen auf die Gestaltung der Infrastruktur un der Stromabnehmer. *Elektrische Bahnen*, 115(2-3), pp. 70-81.
- Bernard, M. (1971). L'Aerodynamique des Trains. *Revue Général des Cheins des Fer*, 90, pp. 80-96.
- Bernard, M. (1995). New Knowledge about Train Resistance at Very High Speed. *French railway techniques*, pp. 31-36.
- Boden, N. (1970). Zur Ermittlung des Luftwiderstandes von Schienenfahrzeugen. *Archiv für Eisenbahntechnik*, 25, pp. 40-71.
- Brockie, N., & Baker, C. (1990). The Aerodynamic Drag of High Speed Trains. *Journal of Wind Engineering and Industrial Aerodynamics*, 34, pp. 273-290, [https://doi.org/10.1016/0167-6105\(90\)90156-7](https://doi.org/10.1016/0167-6105(90)90156-7).
- Buhr, A., & Ehrenfried, K. (2017). High-Speed Particle Image Velocimetry of the Flow around a Moving Train Model with Boundary Layer Control Elements. *Int J of Mechanical, Aerospace, Industrial, Mechatronic and Manufacturing Engineering*, 11(3), pp. 578-586, <http://www.doi.org/10.5281/zenodo.1129573>.
- Carnevale, M., Facchinetti, A., & Rocchi, D. (2016). Assessing Aerodynamic Effects on a Railway Pantograph by means of Computational Fluid Dynamics. *Proceedings of the Third International Conference on Railway Technology*, <https://doi.org/10.4203%2Fccp.110.113>.
- CEN. (2003). *European Standard EN 14067-2:2003 Railway Applications - Aerodynamics, Part 2: Aerodynamics on open track*. Brussels: CEN.
- CEN. (2010). *European Standard EN 14067-6:2010-05 Railway applications - Aerodynamics - Part 6: Requirements and test procedures for cross wind assessment*. Brussels: CEN.
- Coles, D. (1956). The law of the wake in the turbulent boundary layer. *Journal of Fluid Mechanics*, 1, pp. 191-226.
- Crespi, P., Grégoire, R., & Vinson, P. (1994). Laser Doppler Velocimetry Measurements and Boundary Layer Survey On-Board the TGV High Speed Train. *Proceedings of the WCRR 14.-16. November 1994*, 2, pp. 767-773.
- Davis, W. (1926). The Tractive Resistance of Electric Locomotives and Cars. *General Electric Review*, 29(10), pp. 685-707.
- Deeg, P., Jönsson, M., Kaltenbach, H., Schober, M., & Weise, M. (2008). Cross-Comparison of Measurement Techniques for the Determination of Train-Induced Aerodynamic Loads on the Trackbed. *Proceedings of VI International Colloquium on Bluff Bodies Aerodynamics & Applications*. Retrieved from <http://bbaa6.mecc.polimi.it/uploads/treni/BPR04.pdf>
- Erm, L., Jones, M., & Henbest, S. (2012). Boundary Layer Trip Size Selection on Streamlined Bodies of Revolution. *18th Australasian Fluid Mechanics Conference*. Launceston, Australia, 3-7 December. Retrieved from <https://people.eng.unimelb.edu.au/imarusic/proceedings/18/165%20-%20Jones.pdf>
- Fago, B., Lindner, H., & Mahrenholtz, O. (1991). The effect of ground simulation on the flow around vehicles in wind tunnel testing. *Journal of Wind Engineering and Industrial Aerodynamics*, 38, pp. 47-57, [https://doi.org/10.1016/0167-6105\(91\)90026-S](https://doi.org/10.1016/0167-6105(91)90026-S).

- Fey, U., Klein, C., Ondrus, V., Loose, S., & Wagner, C. (2013). Investigation of Reynolds Number Effects in High-Speed Train Wind Tunnel Testing using Temperature-Sensitive Paint. *Rail Aerodynamics*, pp. 29-47. Berlin: IFV Bahntechnik, ISBN 978-3-940727-37-4.
- Firchau, W., Kiekebusch, B., & Neppert, H. (1980). *Grenzschichtdaten für moderne Züge*. Ottobrunn: MBB.
- Fischer, D., Tschepe, J., Nayeri, C., & Paschereit, C. (2018a). Partially-averaged Navier-Stokes method for train aerodynamics. *Proceedings of the 3rd international symposium of rail aerodynamics and train design*.
- Fischer, D., Tschepe, J., Nayeri, C., & Paschereit, C. (2018b). Numerical investigation of high-speed train drag using Partially-averaged Navier-Stokes simulations. *Aerovehicles 3*. Milano, Italy, June 13-15, ISBN 9788894364200.
- Garcia, A. (2010). *High speed, energy consumption and emissions*. Paris: UIC Report. Retrieved from <http://old.uic.org/download.php/publication/526E.pdf>
- Gawthorpe, R. (1978). Aerodynamics of trains in the open air. *Railway Engineer International*, pp. 7-12.
- Gawthorpe, R. (1982). Train drag reduction from simple design changes. *Int. J. of Vehicle Design*, 3(3), pp. 263-274.
- Gaylard, A., Howlett, A., & Harrison, D. (1994). Assessing Drag Reduction Measures for High-Speed Trains. *Proceedings of the Vehicle Aerodynamics Conference of the Royal Aeronautical Society*. Loughborough, UK.
- Haff, J., Schülein, E., Henning, A., Cochard, S., & Loose, S. (2016). Wall Shear Stress Measurements on a Double-Decker Train. *STAB Symposium*. 08.-09. Nov. 2016, Braunschweig, Deutschland.
- Hara, T. (1965). Method of Measuring the Aerodynamic Drag of Trains. *Bulletin of JSME*, 8(31), pp. 390-396.
- Hara, T., Kawaguti, M., Fukuchi, G., & Yamamoto, A. (1968). L'aerodynamique des trains à grand vitesse. *Bulletin de L'A.I. du Congres des Chemins de Fer*, (pp. 364-391). Vienne.
- Hoerner, S. (1965). *Fluid-Dynamic Drag*. Bakersfield, CA: Hoerner Fluid Dynamics.
- Hucho, W. (2012). *Aerodynamik der stumpfen Körper*. Wiesbaden: Vieweg+Teubner. doi:<https://doi.org/10.1007/978-3-8348-8243-1>
- Ido, A. (2015). Energy-saving in conventional trains by aerodynamic drag reduction. *Japanese Railway Engineering*, 188, pp. 2-4.
- Jia, L., Zhou, D., & Niu, J. (2017). Numerical calculation of boundary layers and wake characteristics of high-speed trains with different lengths. *Plos one*. <https://doi.org/10.1371/journal.pone.0189798>
- Jönsson, M., Wagner, C., & Loose, S. (2012b). Underfloor Flow Measurements of 1:50 Generic High-Speed Train Configurations for Different Ground Conditions in a Water Towing Tank. *International Journal of Railway Technology*, 1, pp. 85-113.
- Kapfenberger, W., Flückinger, M., Wili, U., Heland, J., Dumitra, M., Krötz, M., & Höregott, D. (2015). Aerodynamik an Stromabnehmern in kleinen Tunnelquerschnitten - Problem für schnellfahrende Züge? *Elektrische Bahnen*, 113(9), pp. 431-437.
- King, W. F., & Pfitzenmaier, E. (1985). Velocity profiles and pressure fluctuations in the boundary layer on the roof of a railway coach. *Forschung im Ingenieurwesen*, 51, pp. 87-93.
- Kleeberg, J. (2009). New development stage of RHEDA 2000. *Global Railway Review*. Retrieved from <https://www.globalrailwayreview.com/article/124/new-development-stage-of-rheda-2000/>
- Kwon, H., Park, Y., Lee, D., & Kim, M. (2001). Wind tunnel experiments on Korean high-speed trains using various ground simulation techniques. *Journal of Wind Engineering and Industrial Aerodynamics*, 89, pp. 1179-1195. [https://doi.org/10.1016/S0167-6105\(01\)00107-6](https://doi.org/10.1016/S0167-6105(01)00107-6)
- Lai, Y.-C., & Barkan, P. (2005). Options for Improving the Energy Efficiency of Intermodal Freight Trains. *Transportation Research Record*(1916), pp. 47-55.
- Lajos, T., & Preszler, L. (1986). Effect of Moving Ground Simulation on the Flow Past Bus Models. *Journal of Wind Engineering and Industrial Aerodynamics*, 22, pp. 271-277. [https://doi.org/10.1016/0167-6105\(86\)90090-5](https://doi.org/10.1016/0167-6105(86)90090-5)

- Lee, Y., Rho, J., Kim, K., Lee, D., & Kwon, H. (2015). Experimental studies on the aerodynamic characteristics of a pantograph suitable for a high-speed train. *Journal of Rail and Rapid Transit, Proc IMech Part F*, 229, pp. 136-149. <https://doi.org/10.1177%2F0954409713507561>
- Lukaszewicz, P. (2007). Running resistance - results and analysis of full-scale tests with passenger and freight trains in Sweden. *Proc. IMechE Part F: J. Rail and Rapid Transit*, 221, pp. 183-193. <https://doi.org/10.1243%2F0954409JRRT89>
- Lukaszewicz, P. (2009). Running resistance and energy consumption of ore trains in Sweden. *Proc. IMechE Part F: J. Rail and Rapid Transit*, 223, pp. 189-197. <https://doi.org/10.1243%2F0954409JRRT233>
- Maeda, T., Kinoshita, M., Kajiyama, H., & Tanemoto, K. (1989). Aerodynamic Drag of Shinkansen Electric Cars. *QR of RTRI*, 30(1), pp. 48-56.
- Meyer, M., Lerjen, M., Menth, S., & Halder, M. (2008). Das Energiesparprogramm der SBB. *Eisenbahn-Revue*(7), pp. 338-343.
- Miki, T., Hasegawa, Y., & Iai, S. (1959). On the Aerodynamic Problems of High Speed Train. *Bulletin of JSME*, 2(6), pp. 355-364.
- Möbius, B., Wolff, O., Fliege, D., Stoffregen, M., & Westenberger, P. (2017). *Innovationsprogramm Schiene 4.0*. Berlin: Verband der Bahnindustrie. Retrieved from https://bahnindustrie.info/fileadmin/VDB-Positionspapiere/Innovationsprogramm_Schiene_4.0.pdf
- Molland, A., Turnock, S., & Hudson, D. (2011). *Ship Resistance and Propulsion: practical estimation of ship propulsive power*. Cambridge: Cambridge University Press. <https://doi.org/10.1017%2Fcb09780511974113.012>
- Neppert, H. (1984). Komponenten-Widerstände im Einfluß der Grenzschicht an Zügen variabler Länge. *ZEV-Glaser's Annalen*, 9(108), pp. 239-247.
- Niu, J., Liang, X., & Zhou, D. (2016). Experimental study on the effect of Reynolds number on aerodynamic performance of high-speed train with and without yaw angle. *Journal of Wind Engineering and Industrial Aerodynamics*, 157, pp. 36-46. <http://dx.doi.org/10.1016/j.jweia.2016.08.007>
- Nolte, R., & Würtenberger, F. (2003). *Evaluation of Energy Efficiency Technologies for Rolling Stock and Train Operation of Railways*. Berlin: UIC. Retrieved from https://www.izt.de/pdfs/IZT_EVENT_Final_Report.pdf
- Orellano, A., & Kirchhof, R. (2011). Optimising the aerodynamics of high speed trains. *Railway Gazette International*, pp. 41-45.
- Orellano, A., & Sperling, S. (2009). Aerodynamic Improvements and Associated Energy Demand Reduction of Trains. *The Aerodynamics of Heavy Vehicles II: Trucks, Buses, and Trains*, pp. 219-231. https://doi.org/10.1007%2F978-3-540-85070-0_19
- Paradot, N. (2001). *Étude numérique et expérimentale de la résistance à l'avancement d'un train à grande vitesse*. Poitiers: Thèse de doctorat: Mécanique des milieux fluides.
- Paradot, N., Talotte, C., Garen, H., Delville, J., & Bonnet, J.-P. (2002). A Comparison of the Numerical Simulation and Experimental Investigation of the Flow around a High Speed Train. In ASME (Ed.), *Proceedings of ASME FEDSM'02*. Montreal, Quebec, Canada, July 14-18.
- Paz, C., Suárez, E., & Gil, C. (2017). Numerical methodology for evaluating the effect of sleepers in the underbody flow of a high-speed train. *Journal of Wind Engineering and Industrial Aerodynamics*, 167, pp. 140-147. <http://dx.doi.org/10.1016/j.jweia.2017.04.017>
- Peters, J. (1983). Aerodynamics of very high speed trains and maglev vehicles: State of the art and future potential. *International Journal of Vehicle Design*, SP3, pp. 308-341.
- Peters, J. (1990). Bestimmung des aerodynamischen Widerstandes des ICE/V im Tunnel und auf offener Strecke durch Auslaufversuche. *ETR*, 39(9), pp. 559-564.
- Peters, J. (2008). Verloren im Windkanal. *Eisenbahn Geschichte*, 29, pp. 28-37.
- Prandtl, L. (2009). Ergebnisse der Aerodynamischen Versuchsanstalt zu Göttingen. *Göttinger Klassiker der Strömungsmechanik*, 6. <https://doi.org/10.17875/gup2009-103>
- RAPIDE. (2001). *Final Technical Report*.
- Richards, S., & Cooper, R. (1977). *The Measurements of Boundary Layer Profiles on TC2 of APT-E and Assessment of Skin Friction Coefficient*. British Railways Board.

- Rochard, B., & Schmid, F. (2000). A review of methods to measure and calculate train resistances. *Proceedings of the Institution of Mechanical Engineers, Part F: J Rail and Rapid Transit*, 214, pp. 185-199. <https://doi.org/10.1243%2F0954409001531306>
- Roshko, A. (1961). Experiments on the flow past a circular cylinder at very high Reynolds numbers. *J Fluid Mech*, 10, pp. 345-356.
- Sakuma, Y., Suzuki, M., Ido, A., & Kujiyama, H. (2010). Measurement of Air Velocity and Pressure Distributions around High-Speed Trains on Board and on the Ground. *Journal of Mechanical Systems for Transportation and Logistics*, 3(1), pp. 110-118. <https://doi.org/10.1299/jmtl.3.110>
- Schade, H., Kunz, E., Kameier, F., & Paschereit, C. (2013). *Strömungslehre*. Berlin: de Gruyter GmbH. <https://doi.org/10.1515/9783110292237>
- Schetz, J. (2001). Aerodynamics of High-Speed Trains. *Annu. Rev. Fluid Mech.*, 33, pp. 371-414. <https://doi.org/10.1146/annurev.fluid.33.1.371>
- Schlichting, H., & Gersten, K. (2016). *Boundary-Layer Theory*. Berlin Heidelberg: Springer-Verlag. <http://dx.doi.org/10.1007/978-3-662-52919-5>
- Schober, M., Weise, M., Orellano, A., Deeg, P., & Wetzel, W. (2010). Wind tunnel investigation of an ICE 3 endcar on three standard ground scenarios. *Journal of Wind Engineering and Industrial Aerodynamics*, 98, pp. 345-352. <https://doi.org/10.1016/j.jweia.2009.12.004>
- Schoenherr, K. (1932). Resistance of flat surfaces moving through a fluid. *Transactions of the Society of Naval Architects and Marine Engineers*, 40, pp. 279-313.
- Schultz-Grunow, F. (1941). New frictional resistance law for smooth plates. *NASA Tech Memo No. 986*.
- Sforza, P. (2014). *Commercial Airplane Design Principles*. Elsevier. <https://doi.org/10.1016/C2012-0-00332-8>
- Soper, D., Baker, C., Jackson, A., Milne, D., Pen, L. L., Watson, G., & Powrie, W. (2017). Full scale measurements of train underbody flows and track forces. *Journal of Wind Engineering and Industrial Aerodynamics*, 169, pp. 251-264. <https://doi.org/10.1016/j.jweia.2017.07.023>
- Soper, D., Flynn, S., Baker, C., Jackson, A., & Hemida, H. (2018). A comparative study of methods to simulate aerodynamic flow beneath a high-speed train. *Proc IMechE Part F: J Rail and Rapid Transit*, 232(5), pp. 1464-1482. <https://doi.org/10.1177%2F0954409717734090>
- Steuger, M. (2009). Velaro - kundenorientierte Weiterentwicklung eines Hochgeschwindigkeitszuges. *ZEVrail*, 133(10), pp. 414-425.
- Takaishi, T., & Ikeda, M. (2012). Experimental Method for Wind Tunnel Tests to Simulate Turbulent Flow on the Roof of High-Speed Trains. *QR of RTRI*, 53(3), pp. 167-172.
- Tomasini, G., Giappino, S., & Corradi, R. (2014). Experimental investigation of the effects of embankment scenario on railway vehicle aerodynamic coefficients. *Journal of Wind Engineering and Industrial Aerodynamics*, 131, pp. 59-71. <http://dx.doi.org/10.1016/j.jweia.2014.05.004>
- Tropea, C., Yarin, A., & Foss, J. (2007). *Handbook of Experimental Fluid Mechanics*. Berlin: Springer-Verlag. doi:<https://doi.org/10.1007/978-3-540-30299-5>
- Truckenbrodt, E. (2008). *Fluidmechanik Band 2*. Berlin: Springer-Verlag. <https://doi.org/10.1007/978-3-540-79024-2>
- Tschepe, J., Nayeri, C., & Paschereit, C. (2019a). Analysis of moving model experiments in a towing tank for aerodynamic drag measurement of high-speed trains. *Experiments in Fluids*, 60(98). <https://doi.org/10.1007/s00348-019-2748-8>
- Tschepe, J., Maaß, J.-T., & C.N. Nayeri, C. P. (2019b). Experimental investigation of the aerodynamic drag of roof-mounted insulators for trains. *J Rail and Rapid Transit*. <https://doi.org/10.1177/0954409719867537>
- Tschepe, J., Fischer, D., Nayeri, C., Paschereit, C., & Krajnovic, S. (2019c). Investigation of high-speed train drag with towing tank experiments and CFD. *Flow, Turbulence and Combustion*, 102(2), pp. 417-434. <https://doi.org/10.1007/s10494-018-9962-y>
- Tyll, J., D.Liu, J.A.Schetz, & J.F.Marchman. (1996). Experimental Studies of Magnetic Levitation Train Aerodynamics. *AIAA JOURNAL*, 34(12), pp. 2465-2470.

- Wang, S., Burton, D., Herbst, A., Sheridan, J., & Thompson, M. (2018). The effect of the ground condition on high-speed train slipstream. *Journal of Wind Engineering & Industrial Aerodynamics*, 172, pp. 230-243. <https://doi.org/10.1016/j.jweia.2017.11.009>
- White, F. M. (1991). *Viscous Fluid Flow*. New York: McGraw-Hill.
- Willemsen, E. (1997). High Reynolds number wind tunnel experiments on trains. *Journal of Wind Engineering and Industrial Aerodynamics*, pp. 437-447. <https://doi.org/10.1016%2Fs0167-6105%2897%2900175-x>
- Xia, C., Shan, X., & Yang, Z. (2017). Comparison of different ground simulation systems on the flow around a high-speed train. *Proc IMechE Part F: J Rail and Rapid Transit*, 231(2), pp. 135-147. <https://doi.org/10.1177/0954409715626191>
- Yamamoto, T. (2015). Recent Studies and Developments of Energy Saving Technologies in the Field of Railway Vehicles. *QR of RTRI*, 56(4), pp. 235-239.
- Zhang, J., Li, J., Tian, H., Gao, G., & Sheridan, J. (2016). Impact of ground and wheel boundary conditions on numerical simulation of the high-speed train aerodynamic performance. *Journal of Fluids and Structures*, 61, pp. 249-261. <http://dx.doi.org/10.1016/j.jfluidstructs.2015.10.006>
- Zohuri, B. (2015). *Dimensional Analysis and Self-Similarity Methods for Engineers and Scientists*. Switzerland: Springer. <https://doi.org/10.1007/978-3-319-13476-5>
- Zurrel, C. (2004). *Aerodynamics of circular cylinders inclined to airflow and wind-induced vibrations of dry inclined cable at high wind speeds*. Ottawa, Canada: University of Ottawa. <http://dx.doi.org/10.20381/ruor-19636>